

Accepted for Publication in The Astrophysical Journal

Hubble Space Telescope Observations of Element Abundances in Low-redshift Damped Lyman- α Galaxies and Implications for the Global Metallicity-Redshift Relation

Varsha P. Kulkarni

Dept. of Physics & Astronomy, University of South Carolina, Columbia, SC 29208

S. Michael Fall

Space Telescope Science Institute, Baltimore, MD 21218

James T. Lauroesch

Department of Physics & Astronomy, Northwestern University, Evanston, IL 60208

Donald G. York ¹ and Daniel E. Welty

Dept. of Astronomy & Astrophysics, University of Chicago, Chicago, IL 60637

Pushpa Khare

Dept. of Physics, Utkal University, Bhubaneswar, India

James W. Truran ¹

Dept. of Astronomy & Astrophysics, University of Chicago, Chicago, IL 60637

ABSTRACT

Most models of cosmic chemical evolution predict that the mass-weighted mean interstellar metallicity of galaxies should rise with time from a low value $\sim 1/30$ solar at $z \sim 3$ to a nearly solar value at $z = 0$. In the absence of any selection effects, the damped Lyman-alpha absorbers (DLAs) in quasar spectra are expected to show such a rise in global metallicity. However, it has been difficult to determine whether or not DLAs show this effect, primarily because of the very small number of DLA metallicity measurements at low redshifts.

¹Also, the Enrico Fermi Institute, University of Chicago, Chicago, IL 60637

In an attempt to put tighter constraints on the low-redshift end of the DLA metallicity-redshift relation, we have observed Zn II and Cr II lines in four DLAs at $0.09 < z < 0.52$, using the Space Telescope Imaging Spectrograph (STIS) onboard the Hubble Space Telescope (HST). These observations have provided the first constraints on Zn abundances in DLAs with $z < 0.4$. In all the three DLAs for which our observations offer meaningful constraints on the metallicity, the data suggest that the metallicities are much lower than the solar value. These results are consistent with recent imaging studies indicating that these DLAs may be associated with dwarf or low surface brightness galaxies.

We combine our results with higher redshift data from the literature to estimate the global mean metallicity-redshift relation for DLAs. We find that the global mean metallicity shows at most a slow increase with decreasing redshift. For the redshift range $0.09 < z < 3.90$, the slope of the exponential fit to the binned $N(\text{HI})$ -weighted mean Zn metallicity vs. redshift relation is -0.18 ± 0.06 counting Zn limits as detections, -0.22 ± 0.08 counting Zn limits as zeros, and -0.23 ± 0.06 using constraints on metallicity from other elements in cases of Zn limits. The corresponding estimates of the $z = 0$ intercept of the metallicity-redshift relation are -0.74 ± 0.15 , -0.75 ± 0.18 , and -0.71 ± 0.13 , respectively. Roughly similar results are obtained if survival analysis or an unbinned $N(\text{HI})$ -weighted nonlinear χ^2 approach is used. Thus, the $N(\text{HI})$ -weighted mean metallicity of DLAs does not appear to rise up to solar or near-solar values at $z = 0$. This weak evolution could be explained by the fact that our absorption-selected sample seems to be dominated by dwarf or low surface brightness galaxies. This suggests that current DLA samples, especially those at low redshifts, could be biased against more enriched galaxies because the latter may cause higher dust obscuration of the background quasars.

Subject headings: quasars: absorption lines; galaxies: evolution; galaxies: abundances; cosmology: observations

1. Introduction

A great deal of progress has been made in recent years in the observations of high-redshift galaxies. The average star formation history of the Universe has been estimated from emission properties of galaxies detected in deep imaging and redshift surveys (e.g., Lilly et al. 1996; Madau et al. 1996). This emission history of galaxies is tied intimately to the history of gas consumption and metal production in galaxies, because the global

mean densities of gas, metals, and stars are coupled through conservation-type relations. Constraining the history of metal production thus puts constraints on the histories of star formation and gas consumption (e.g., Pei & Fall 1995).

Most models of cosmic chemical evolution, ranging from analytical calculations to numerical simulations, predict the mass-weighted mean global metallicity in galaxies, given by $\Omega_{\text{metals}}^{\text{ISM}}/\Omega_{\text{gas}}^{\text{ISM}}$, to rise from a low value at high redshift to a near-solar value at zero redshift (e.g., Pei & Fall 1995; Malaney & Chaboyer 1996; Pei, Fall, & Hauser 1999; Somerville, Primack, & Faber 2001; Tissera et al. 2001). [Here $\Omega_{\text{metals}}^{\text{ISM}}$ and $\Omega_{\text{gas}}^{\text{ISM}}$ refer, respectively, to the mean comoving density of metals and the total mean comoving density of gas in the interstellar matter of galaxies, both measured in units of the present critical density ($\rho_c = 3H_0^2/8\pi G$).] The present-day mass-weighted mean metallicity of local galaxies is also observed to be close to solar (e.g., Kulkarni & Fall 2002). It is therefore of great interest to determine whether element abundance measurements in galaxies actually show the predicted rise in mean metallicity with time.

Abundance measurements in quasar absorption systems can directly probe the history of metal production in galaxies. Particularly useful in this respect are the damped Lyman- α (DLA) absorbers ($\log N_{\text{HI}} \geq 20.3$). Under reasonable assumptions, DLAs may contain enough neutral gas to form a large fraction of the stars visible today (Wolfe et al. 1995). DLAs are our principal source of information about the chemical content of interstellar matter in high- z galaxies (e.g., Meyer & York 1992; Lu et al. 1996; Kulkarni et al. 1996, 1997, 1999; Pettini et al. 1994, 1997, 1999; Prochaska & Wolfe 1999; Prochaska et al. 2001a, 2003a, 2003b; and references therein).

For a variety of reasons, the abundance of Zn is often taken as the metallicity indicator in DLAs. Zn tracks Fe closely, to within $\sim \pm 0.1$ dex, in Galactic halo and disk stars for metallicities $[\text{Fe}/\text{H}] \gtrsim -3$ (e.g., Mishenina et al. 2002; Cayrel et al. 2004; Nissen et al. 2004). Zn is also relatively undepleted on interstellar dust grains, so that gas-phase Zn abundances can give metallicity estimates relatively free of depletion effects. Finally, Zn II has two absorption lines at $\lambda\lambda 2026, 2062$ that, in DLAs, often lie outside the Lyman- α forest and are usually unsaturated. There are, however, some uncertainties related to the nucleosynthesis of Zn and the potential role of ionization corrections, and we return to these issues in section 5.1.

The absorption lines of DLAs sample the interstellar matter of distant galaxies. This sampling is completely independent of many properties of the galaxies, including their luminosities, sizes, and morphologies. It can be shown (e.g., Lanzetta, Wolfe, & Turnshek 1995; Kulkarni & Fall 2002) that, in the absence of selection effects, the quantity $\Omega_{\text{metals}}^{\text{ISM}}/\Omega_{\text{gas}}^{\text{ISM}}$ in

galaxies is equal to the N_{HI} -weighted mean metallicity \bar{Z} in a sample of DLAs, given by

$$\bar{Z} = \frac{\sum N(\text{Zn II})_i / \sum N(\text{HI})_i}{(\text{Zn/H})_{\odot}} Z_{\odot}. \quad (1)$$

This quantity \bar{Z} may therefore be expected to show a rise from a low value at high redshift to a near-solar value at low redshift.

There has been great debate about this issue in the past few years, with most studies advocating no evolution in the global mean metallicity \bar{Z} inferred from DLAs (e.g., Pettini et al. 1997, 1999; Prochaska & Wolfe 1999, 2000; Vladilo et al. 2000; Savaglio 2001; Prochaska, Gawiser, & Wolfe 2001b). Kulkarni & Fall (2002) examined this issue further by applying various statistical analyses to the Zn data from the literature. Based on a compilation of 57 Zn measurements (36 detections and 21 limits) from the literature at redshifts $0.4 < z < 3.4$, Kulkarni & Fall (2002) found the slope of the metallicity-redshift relation to be -0.26 ± 0.10 , consistent at $\approx 2 - 3\sigma$ level with both the predicted rates of evolution (-0.25 to -0.61), and with no evolution. Recently, Prochaska et al. (2003b) have reached similar conclusions (slope -0.25 ± 0.07) for $0.5 < z < 4.7$, using Zn measurements in 11 DLAs and Fe, Si, S, or O measurements in 110 other DLAs. As in the case of Zn, the elements Fe, Si, S, and O also have both advantages (e.g., better theoretical understanding of nucleosynthesis, ease of detection) and disadvantages [e.g., dust depletion (for Fe, Si), lack of two or more weak lines outside the Lyman-alpha forest (for Si, S, O), potential ionization effects (for Si, S), potential enhancement with respect to the Fe-group elements due to alpha enrichment (for Si, S, O), etc.]. In any case, the results of Prochaska et al. (2003b), based on these other elements, are similar to those of Kulkarni & Fall (2002), as discussed further in section 4.

The issue of metallicity evolution in DLAs is still not fully understood. The main reason for the debate about this issue is the small number of measurements available, especially at $z < 1.5$. The samples of Kulkarni & Fall (2002) and Prochaska et al. (2003b) both include only 1 measurement each in the redshift range $z \lesssim 0.6$, which corresponds to $> 40\%$ of the age of the Universe. The low-redshift systems require space-based ultraviolet (UV) measurements to access the H I lines at $z < 1.6$ and the Zn II lines at $z < 0.6$. With the goal of putting better constraints on the low-redshift end of the DLA metallicity-redshift relation, we have obtained UV spectra of three quasars with four intervening DLAs at $0.09 < z < 0.52$ using the Space Telescope Imaging Spectrograph (STIS) onboard the *Hubble Space Telescope (HST)*. Here we report our new observations of the Zn II and Cr II absorption in these low-redshift DLAs and their implications for the metallicity-redshift relation for DLAs. We have chosen to focus on Zn as the primary metallicity indicator, rather than combine measurements of Zn with those of Si or S, primarily because (a) we prefer to use the more uniform Zn sample, relatively free of assumptions about dust depletion, and (b) STIS is much more sensitive at the longer

wavelengths of the Zn II lines than at the wavelengths of the S II and Si II lines for our DLAs. Section 2 describes our observations and data reduction. Section 3 describes the results for the individual DLAs. Section 4 presents the implications of our results, combined with higher redshift data from the literature, for the metallicity-redshift relation of DLAs. Section 5 discusses the advantages and disadvantages of using Zn, the morphological information for the galaxies giving rise to the DLAs in our sample, and potential selection effects. Finally, section 6 provides a summary of our results.

2. Observations and Data Reduction

2.1. Observations

Our sample consists of 4 confirmed DLAs with $0.09 < z < 0.52$ and $\log N_{\text{HI}} \gtrsim 20.3$ in the sightlines toward the quasars Q0738+313, Q0827+243, and Q0952+179. Table 1 lists the key properties of these DLAs known from previous studies. The lines of interest are Zn II $\lambda\lambda$ 2026.136, 2062.664, and Cr II $\lambda\lambda$ 2056.254, 2062.234, 2066.161, which occur in the range of 2211-3145 Å for the DLAs in our sample.

Our observations were obtained during February–November 2003 using *HST* STIS. Table 2 summarizes the details of our observations. The STIS near-ultraviolet Multi-Anode Microchannel Array (nuv-MAMA) was used for Q0738+313 and Q0952+179. For Q0827+243, the CCD was used because of its higher efficiency at the longer wavelengths required for this object. The first-order gratings G230M and G230MB were used to get the moderately high spectral resolution and wavelength coverage necessary for the abundance determinations. The $52'' \times 0.2''$ slit was used for the MAMA observations to achieve a good compromise between spectral resolution and throughput. For the CCD, the 52x0.2E1 pseudo-aperture (with the default target placement near row 893, $\sim 5''$ from the top of the CCD) was used to mitigate the effects of the charge-transfer inefficiency.

All targets were acquired with the F28x50LP aperture using the STIS CCD in the acquisition mode. Acquisition exposures of 3–5 s were used to achieve a signal-to-noise ratio (SNR) of > 40 , taking care not to saturate the detector. The science exposures were dithered using the “STIS-ALONG-SLIT” pattern in 3, 4, or 5 steps of $0.4''$ each, so as to help with flatfielding and removal of hot pixels. For the CCD observations, the exposures at each dithered setting were divided into 3 equal subexposures with CR-SPLIT=3 to facilitate the rejection of cosmic rays. An automatic wavelength calibration exposure at the respective grating setting was included in each orbit.

2.2. Data Reduction

All data reduction tasks were performed independently by two members of our team, using multiple techniques as discussed below. The spectra were reduced using the Image Reduction and Analysis Facility (IRAF) version 2.12.1 and the CALSTIS package in the Space Telescope Science Data Analysis System (STSDAS) software version 3.1. The automatic lamp exposures obtained during our observations were used for wavelength calibration. For all other calibrations, the most recent reference files available in the *HST* data archives were used. These include image reference files for darks, pixel-to-pixel flat fields, low-order flat fields, tables for aperture description, aperture throughput, bad pixels, dispersion coefficients, incidence angle correction, and image distortion correction for both the MAMA and the CCD. In addition, the CCD reductions required the bias calibration files from the *HST* archives. For the MAMA, other calibration files included tables for linearity, offset correction, scattered light correction, near-UV dark correction, and time-dependent sensitivity correction.

After the initial reduction of each 2-dimensional image, the spectral extraction was carried out using the STSDAS task X1D. In order to obtain optimum signal-to-noise ratios in the 1-dimensional spectra, a variety of extraction heights were tested. Extraction heights of 3 or 4 pixels were found to encompass all of the recoverable flux without introducing additional noise from the background. The results of X1D were checked by repeating the spectral extractions with the IRAF task APALL. In these latter reductions, the sky background level was fitted in the regions on either side of the quasar spectrum, and this fit used to subtract the background level. In most cases, second-order Chebyshev polynomials were found to provide adequate fits to the traces of the spectra. The results of these various reductions were found to be in very close agreement. Finally, for each target, the individual 1-dimensional spectra at each wavelength setting were combined together. The combined spectra were then continuum-fitted using Chebyshev or cubic spline functions of orders 2 to 6, depending on the shape of the continuum and the presence or absence of broad emission lines in the wavelength range observed. Figs. 1-5 show the continuum-normalized intensity versus vacuum wavelength for all the targets. The spectral dispersions are $0.09 \text{ \AA pixel}^{-1}$ for the NUV-MAMA spectra, and $0.15 \text{ \AA pixel}^{-1}$ for the CCD spectra. The resulting spectral resolutions are in the range of $\approx 21 - 24 \text{ km s}^{-1}$ for the NUV-MAMA data and $\approx 29 \text{ km s}^{-1}$ for the CCD data.

Table 3 lists the features measured in the final spectra. The central wavelengths and equivalent widths were measured using the IRAF task SPLOT. The 1σ uncertainties in equivalent widths due to photon noise were estimated assuming Poisson statistics as $\sigma_W^p = \Delta\lambda\sqrt{N_{pix}}/SNR$ where $\Delta\lambda$ is the spectral dispersion, N_{pix} is the number of pixels occupied

by the feature, and SNR is the signal-to-noise ratio per pixel in the continuum near the feature.

Another uncertainty often not considered in spectroscopic studies of QSO absorption line systems is the uncertainty in the equivalent width (and hence column density) associated with the continuum placement (e.g., Savage & Sembach 1991). While the continua of QSOs are in general much simpler than the stellar continua encountered in studies of the Galactic interstellar matter, there is still some uncertainty associated with the exact placement of the continuum. In order to assess this uncertainty, we slid the continuum up and down by 0.3 times the 1σ noise level and measured the equivalent widths for these extrema (see Sembach & Savage 1992 for a justification of the scale factor 0.3). Table 4 lists the continuum placement uncertainties in the equivalent widths σ_W^c thus calculated for the DLA metal features. Also listed are the total uncertainties σ_W^t calculated by adding the photon noise uncertainties and continuum uncertainties in quadrature. Further details on the line measurements are provided in section 3.

2.3. Estimation of Column Densities

Column densities for Zn II and Cr II were estimated by fitting the observed absorption line profiles using the program FITS6P (Welty, Hobbs, & York 1991) that evolved from the code used by Vidal-Madjar et al. (1977). FITS6P minimizes the χ^2 between the data and the theoretical Voigt profiles convolved with the instrumental profile. The atomic data were adopted from Bergeson & Lawler (1993) for Zn II $\lambda \lambda 2026, 2062$ and Cr II $\lambda \lambda 2056, 2062, 2066$, and from Bergeson, Mullman, & Lawler (1994) for Fe II $\lambda \lambda 2249, 2260$. The oscillator strengths used for these lines were 0.489, 0.256 for Zn II $\lambda \lambda 2026, 2062$; 0.105, 0.078, 0.0515 for Cr II $\lambda \lambda 2056, 2062, 2066$; and 0.00182, 0.00244 for Fe II $\lambda \lambda 2249, 2260$.

In an attempt to constrain the column densities and effective Doppler b parameters, we performed simultaneous single-component fits to the detected lines of Zn II, Cr II, and Fe II (where available), varying the column densities N , the Doppler parameter b , and the central velocity v together, but assuming a common b and v value for Zn II, Cr II, and the weak Fe II lines. We also performed simultaneous single-component fits to both detected and undetected lines. The uncertainties in N , b , and v were determined simultaneously in these fits.

In the cases where a 2026 Å feature was potentially present, we investigated its contribution by carrying out profile fits with the Mg I $\lambda 2026$ line included. To do this, the Mg I column density was estimated from profile fitting of the Mg I $\lambda 2853$ feature in data obtained

at the Multiple Mirror Telescope (MMT), if available (Khare et al. 2004). The MMT data were obtained as part of a larger survey of element abundances in DLAs at $z < 1.5$. These data have lower spectral resolution ($\sim 75 - 95 \text{ km s}^{-1}$) but higher SNR ($\sim 50 - 90$). The Mg I $\lambda 2026$ line was found to make insignificant contribution to the observed 2026 Å feature. Indeed, there is no evidence of absorption at the expected positions of Mg I $\lambda 2026$ in any of the 3 DLAs where the relevant wavelength region was covered.

The best-fit effective b values were found to be in the range of 11-15 km s^{-1} . However, due to the moderate resolution and SNR of our data and the weakness of the lines, it was difficult to derive accurate estimates for the effective b values. Therefore, in order to explore the dependence of the estimated column densities on the b values, we also performed single-component fits to the individual detected lines for several (fixed) choices of b , i.e., 5, 10, 15, and 20 km s^{-1} . In general, relatively little difference in column density was found for the fits with b -values of 5-20 km s^{-1} , indicating that the lines would be near the linear part of the curve of growth for that range in effective b . To search for any broad, shallow components that could be hidden in the noise, we also examined all the spectra after smoothing them by a factor of 3. No broad and shallow components could be discerned.

The only other available information relevant to the effective b values for the DLAs in our sample is from the H I 21 cm absorption lines (Chengalur & Kanekar 1999; Kanekar & Chengalur 2001) and/or from lines of Ca II or Mg II seen in our MMT data for these systems (Khare et al. 2004). While the latter data cannot be used to estimate the b -values of individual components accurately, they provide upper limits to the effective b -values, and indicate a spread in velocities of several tens of km s^{-1} . Further details on the b values are provided in discussions of the individual systems in section 3. The total column densities obtained with the present resolution are expected to be close to the actual values if very strongly saturated components are not present (Jenkins 1986). It seems unlikely that any of our Zn II, Cr II, or Fe II lines consist of single components with b -values less than 5 km s^{-1} . Indeed, b values $\leq 5 \text{ km s}^{-1}$ for the dominant component contributing to the Zn II lines are found in none of the eight DLAs at $z < 1.5$ and only $\approx 20\%$ of the 24 DLAs at $z < 3.4$ for which profile fits from high-resolution data are available in the literature (Lu et al. 1995; Meyer et al. 1995; Prochaska & Wolfe 1997; Lopez et al. 1999; Pettini et al. 1999, 2000; de la Varga et al. 2000; Molaro et al. 2001; Ellison & Lopez 2001; Ledoux et al. 2002; Levshakov et al. 2002; Peroux et al. 2002; Ledoux et al. 2003; Dessauges-Zavadsky et al. 2003, 2004). Thus, it would be unusual, although not impossible, in a sample of four low-redshift DLAs, to find two or more with $b < 5$. [Of course, it is possible that the low incidence of systems with $b < 5 \text{ km s}^{-1}$ is a reflection of the limited resolution ($\approx 6-8 \text{ km s}^{-1}$ at best) achieved so far for DLA spectra with current instrumentation. In principle, if DLAs often contain significant narrow, unresolved components, then many existing column density

estimates for heavy elements in DLAs could be too low.] It would be desirable to have higher resolution observations in the future to understand the detailed component structure. This would need a large amount of observing time on a space-based telescope.

In order to evaluate the effect of continuum placement uncertainties on our column density estimates, we slid the continuum up and down by 0.3 times the 1σ noise level and measured the column densities for these extrema by refitting the lines with FITS6P. This was then used to calculate the uncertainty in the column densities due to the continuum placement uncertainty, which was then added in quadrature with the errors associated with the photon noise, uncertainty in b -values, and uncertainty in component velocities to derive the final errors.

Finally, we also estimated the column densities using the apparent optical depth (AOD) method (see, e.g., Savage & Sembach 1991). The column densities obtained using this method were consistent with those obtained from profile fitting within the mutual 1σ uncertainties. However, the AOD results are expected to be less accurate than the profile-fitting approach for our data because of the relatively low SNR and resolution. This is because the AOD method weights all points across the observed profile equally, i.e., it does not take into account the fact that the observed profile “should” resemble the instrumental profile if the lines are unresolved or marginally resolved. Thus, for example, outlying downward noise points could spuriously increase the computed AOD column density. We thus adopted the profile-fitting estimates of the Zn II, Cr II, and Fe II column densities and combined these with the known H I column densities to estimate the element abundances. For reference, we adopted the solar abundances recommended by Lodders (2003).

3. Results

3.1. Q0738+313

This quasar ($z_{em} = 0.635$) has two strong DLAs at $z = 0.0912$ and $z = 0.2212$ with $\log N_{\text{HI}} = 21.18^{+0.05}_{-0.06}$ and $\log N_{\text{HI}} = 20.90^{+0.07}_{-0.08}$, respectively (Rao & Turnshek 1998). The $z = 0.2212$ system was known to be an Mg II absorber and identified as a DLA on the basis of *HST* UV spectra (Rao & Turnshek 1998). The $z = 0.0912$ absorber was discovered serendipitously in the same *HST* UV data. The quasar also shows 21-cm absorption at the redshifts of both the DLAs (Lane et al. 1998; Chengalur & Kanekar 1999). The Zn II and Cr II lines of both systems lie outside the Ly- α forest. The wavelength coverage achieved with three separate grating settings included all five lines of Zn II and Cr II for each DLA. The “unidentified” features near 2155, 2187, and 2217 Å are likely to be C IV λ 1548 lines

at $z = 0.392$, 0.413 , and 0.432 , respectively, with the corresponding $\lambda 1551$ features lost in the noise.

3.1.1. The $z = 0.0912$ DLA

Fig. 6 shows the velocity profiles of the Fe II, Zn II, and Cr II data for this DLA. The zero point of the velocity scale refers to the absorption redshift $z = 0.0912$ inferred from the 21-cm and optical data. Counting both photon noise and continuum uncertainties, our data show weak $\approx 2.8 \sigma$, 2.7σ , and 3.3σ features, respectively, at the wavelengths of the Zn II $\lambda 2026$, Cr II $\lambda 2056$, and Fe II $\lambda 2260$ lines. No other lines of these species were detected in our *HST* spectra. The 21-cm absorption in this object has been observed to be dominated by a single component at $z = 0.09118 \pm 0.00001$ with a full width at half maximum (FWHM) of $\sim 5 \text{ km s}^{-1}$, indicating a Doppler parameter $b_{21\text{cm}} = 3.0 \text{ km s}^{-1}$ for cold, neutral hydrogen (Chengalur & Kanekar 1999).¹ Based on our complementary MMT spectra (Khare et al. 2004), we derive effective $b < 42 \text{ km s}^{-1}$ for Ca II.

We first carried out profile fits using only the potentially detected lines Zn II $\lambda 2026$, Cr II $\lambda 2056$, and Fe II $\lambda 2260$. The fits were then repeated by fitting these lines together with the undetected lines Zn II $\lambda 2062$; Cr II $\lambda \lambda 2062, 2066$; and Fe II $\lambda 2249$. To be conservative, we adopt the results from these latter fits, and list the derived Zn II, Cr II, and Fe II column densities, and the corresponding abundances in Table 5. The error bars on column densities and abundances for these fits include uncertainties from Poisson statistics and uncertainties in b value, central velocity, and continuum placement. The formal estimate of the best fit Zn II column density in this DLA has a relatively large total error, therefore we list it only as a 3σ upper limit. To explore the dependence of the estimated column densities on the b values, we also performed single-component fits to the individual detected lines for several (fixed) choices of b , i.e., 5, 10, 15, and 20 km s^{-1} , which are also listed in Table 5. The column densities for these single line fits with b fixed are higher than that for the multiple-line fit with N, b, v varied, because the former included fits to only detected lines, while the latter included fits to both detected and undetected lines.

The dashed curves in Fig. 6 show the profiles for the best-fit N , b , and v parameters obtained by varying these parameters simultaneously for the multiple lines stated above. The estimate of b value obtained in this way is $11.2 \pm 6.7 \text{ km s}^{-1}$, where the uncertainties in

¹The Zn II, Cr II, and Fe II lines can arise in warmer H I gas or even H II regions, and could thus have effective b -values different from $b_{21\text{cm}}$. (If H II regions are present, the derived abundances $[X/H]$ would, strictly speaking, be upper limits.)

b were calculated simultaneously with the uncertainties in N and v .

For pictorial illustration, we created simulations of the Zn II λ 2026 line for solar, 32 % solar, and 10 % solar metallicities ($[Zn/H] = 0.0, -0.5, \text{ and } -1.0$), assuming the best-fit b and v values, $b = 11.2 \text{ km s}^{-1}$ and $v = 9.9 \text{ km s}^{-1}$. These simulations are shown in Fig. 7, overlaid on top of our data, and support the profile fitting results that the metallicity appears to be low.

3.1.2. The $z = 0.2212$ DLA

This DLA has also been detected in 21-cm absorption. Kanekar, Ghosh, & Chengalur (2001) have reported three components in the 21-cm absorption line, the dominant one having FWHM = 18.6 km s^{-1} and comprising $\sim 87\%$ of the H I column density. This indicates a Doppler parameter $b_{21\text{cm}} = 11.2 \text{ km s}^{-1}$ for most of the cold, neutral hydrogen. Our MMT data suggest effective $b \leq 38 \text{ km s}^{-1}$ for Mg I and Mg II in this DLA (Khare et al. 2004).

Fig. 8 shows the velocity profiles of the Zn II and Cr II data for this DLA. The zero point of the velocity scale refers to the absorption redshift $z = 0.2212$ inferred from the 21-cm and optical data. Our data show $\approx 2.8 \sigma$ and 3.5σ features at the wavelengths of the Cr II λ 2062 and Zn II λ 2062 lines. These lines lie in the C IV broad emission line of the quasar, and therefore have higher continuum SNR than that for the Zn II λ 2026 and Cr II λ 2056 lines which are not detected.

We first carried out profile fits using the potentially detected lines Zn II λ 2062 and Cr II λ 2062 together with the undetected line Cr II λ 2066. The undetected Zn II λ 2026 and Cr II λ 2056 lines were not included in the fits because they lie in regions of the spectrum with lower continuum signal level. The estimate of the b value obtained in this way is $12.2 \pm 7.7 \text{ km s}^{-1}$. In Table 6, we list the derived Zn II and Cr II column densities, and the corresponding abundances. The dashed curves in Fig. 8 show the profiles for these best-fit N , b , and v parameters. Also listed in Table 6 are results of single-component fits to the individual detected lines for several (fixed) choices of b , i.e., 5, 10, 15, and 20 km s^{-1} . The column densities of Cr II for these single line fits with b fixed are higher than that for the multiple-line fit with N, b, v varied, because the former included only the detected lines (Cr II λ 2062, Zn II λ 2062), while the latter also included the undetected Cr II λ 2066 line.

We next checked whether the Zn II and Cr II column densities thus estimated are consistent with the lack of significant features at the positions of the Zn II λ 2026 and Cr II λ 2056 lines in the noisier parts of our spectra. To do this, we generated simulated Zn II

$\lambda 2026$ and Cr II $\lambda 2056$ lines with the best-fit parameters estimated from the Cr II $\lambda \lambda 2062, 2066$ and Zn II $\lambda 2062$ lines. At our resolution, the Zn II $\lambda 2026$ and Cr II $\lambda 2056$ features would be 7 pixels wide, but are lost in the noise. The 3σ limits on the rest-frame equivalent width over these 7-pixel wide simulated features are about 89 mÅ and 75 mÅ, respectively, at the positions of the Zn II $\lambda 2026$ and Cr II $\lambda 2056$ lines. For the best-fit b value of 12.2 km s⁻¹, this implies 3σ upper limits of $\log N_{\text{ZnII}} < 12.81$, i.e. $[\text{Zn}/\text{H}] < -0.72$, and $\log N_{\text{CrII}} < 13.37$, i.e. $[\text{Cr}/\text{H}] < -1.18$. These limits are consistent with the values obtained from the data for Zn II $\lambda 2062$ and Cr II $\lambda \lambda 2062, 2066$. Thus the Zn abundance in this system is likely to be close to -0.70, the value obtained from the $\lambda 2062$ line. Nevertheless, to be conservative, we adopt an upper limit $[\text{Zn}/\text{H}] \leq -0.70$ for this system.

For pictorial illustration, we show in Fig. 9 simulations of the Zn II $\lambda 2062$ line for solar, 32% solar, and 10% solar metallicities ($[\text{Zn}/\text{H}] = 0.0, -0.5, \text{ and } -1.0$), assuming the best-fit b and v values, $b = 12.2$ km s⁻¹ and $v = 15.3$ km s⁻¹. The parameters of the Cr II $\lambda 2062$ line are held fixed in these simulations, as determined from the best-fit obtained by fitting together the Cr II $\lambda \lambda 2062, 2066$, Zn II $\lambda 2062$ lines. These simulations support the profile fitting results that the metallicity appears to be low.

3.2. Q0827+243

This quasar ($z_{em} = 0.939$) has a DLA at $z = 0.5247$ with $\log N_{\text{HI}} = 20.30_{-0.05}^{+0.04}$ (Rao & Turnshek 2000). The system was known from ground-based studies as a strong Mg II absorber at $z = 0.5247$, and found to be a DLA in *HST* UV spectra (Rao & Turnshek 2000). The quasar also shows a relatively broad and possibly multi-component 21-cm absorption feature at $z = 0.52476 \pm 0.00005$, with FWHM ~ 50 km s⁻¹, indicating $b_{21\text{cm}} \sim 30$ km s⁻¹ in the cold neutral hydrogen (Kanekar & Chengalur 2001). Our MMT data show Fe II and Mn II absorption at $z = 0.5249$, with an effective $b \leq 35$ km s⁻¹ (Khare et al. 2004).

Unfortunately, this quasar was in a significantly fainter state at the time of our *HST* observations than expected from previous UV data. Therefore the SNR in our *HST* data was poorer than expected. The wavelength region covered all five lines of Zn II and Cr II, but no lines could be detected. Fig. 10 shows the velocity profiles for this DLA. The zero point of the velocity scale refers to the absorption redshift $z = 0.5247$ inferred from the 21-cm and optical data. Although weak features are seen at -20 km s⁻¹ in the Cr II $\lambda 2062$ line and possibly at -40 km s⁻¹ in the Zn II $\lambda 2062$ line, they are comparable to the noise. Furthermore, there is no evidence for these features in the stronger Zn II $\lambda 2026$ or Cr II $\lambda 2056$ lines. The 3σ rest frame equivalent width limits in our *HST* data at the expected positions of the Zn II $\lambda 2026$ and Cr II $\lambda 2056$ lines are 96 mÅ and 90 mÅ, respectively.

The corresponding 3σ upper limits on the Zn II and Cr II column densities and abundances are listed in Table 7 for $b = 5, 10, 15,$ and 20 km s^{-1} . The differences between the limits for $b = 15$ and 20 are small, so the limits for higher b -values are expected to be close to those for $b = 20 \text{ km s}^{-1}$. For example, for $b = 30$, the b value of the 21-cm absorption line, the limits are about 0.1 dex lower than for $b = 10$. The dashed curves in Fig. 10 show the profiles corresponding to the 3σ upper limits for $b = 10$.

The low SNR of our STIS data for Q0827+243 prevents us from putting tight constraints on the Zn and Cr abundances in the DLA absorber along this sightline. We note that based on MMT spectra of this target, the abundance of Fe in this DLA is $[\text{Fe}/\text{H}] = -1.02 \pm 0.05$ (Khare et al. 2004). The total (gas + solid phase) metallicity could of course be higher. But the DLA toward this quasar has a much lower N_{HI} than that of the other three DLAs in our sample. Therefore, unless the metallicity of this DLA is substantially supersolar (which would imply a very large amount of dust depletion), it would not significantly affect our estimates of the global metallicity of DLAs at low redshifts, which anyway treat this DLA as an upper limit.

3.3. Q0952+179

This quasar ($z_{em} = 1.472$) has a strong DLA at $z = 0.2378$ with $\log N_{\text{HI}} = 21.32^{+0.05}_{-0.06}$ (Rao & Turnshek 2000). The absorber was known to be a strong Mg II system and found to be a DLA in *HST* UV spectra (Rao & Turnshek 2000). The quasar also shows 21-cm absorption at the same redshift (Kanekar & Chengalur 2001).

Our wavelength setting covered the Zn II λ 2062 and Cr II $\lambda\lambda$ 2056, 2062, 2066 lines. A separate setting to cover only the Zn II λ 2026 line was not obtained in view of the large number of orbits needed for this faint quasar to cover even a single grating setting to a reasonable SNR. Tables 3 and 4 list the lines measured in the final spectrum. Fig. 11 shows the velocity profiles for the Zn II and Cr II lines in this absorber. The zero point of the velocity scale refers to the absorption redshift $z = 0.2378$ inferred from the 21-cm and optical data. Our data show weak 2.5σ , 4.2σ , and 2.1σ features at the wavelengths of the Cr II λ 2056, Cr II λ 2062, and Zn II λ 2062 lines. The strong feature appearing near 200 km s^{-1} in the Cr II λ 2056 line cannot be Cr II, because it is not seen in the Cr II λ 2062 line (which is lower in f value by a factor of only 1.3) even though the SNR in the continuum is comparable. Furthermore, the velocity of this component would be too high compared to the redshifts of the Mg II and 21-cm absorption lines. We take this feature to be a Lyman- α forest line.

The only other metal lines available in the literature for this DLA are the Mg II $\lambda\lambda$ 2796, 2803 lines at $z = 0.2378$ in lower resolution spectra. The 21-cm absorption line detected by Kanekar & Chengalur (2001) at $z = 0.23780 \pm 0.00002$ shows a single component with a FWHM of 7.7 km s^{-1} , indicating $b_{21\text{cm}} = 4.6 \text{ km s}^{-1}$ for cold neutral hydrogen.

We carried out profile fits using simultaneously all the lines of Zn II and Cr II that were included in our data, i.e., Zn II λ 2062 and Cr II $\lambda\lambda$ 2056, 2062, 2066. The dashed curves in Fig. 11 show the profiles for the best-fit N , b , and v parameters. The estimate of the b value obtained from the fits is $15.0 \pm 7.7 \text{ km s}^{-1}$. In Table 8, we list the derived Zn II and Cr II column densities, and the corresponding abundances. The formal estimate of the best fit Zn II column density in this DLA has a relatively large total error; therefore we list it only as a 3σ upper limit. Also listed in Table 8 are results of single-component fits to the individual detected lines for several (fixed) choices of b , i.e., 5, 10, 15, and 20 km s^{-1} .

For illustrative purposes we show, in Fig. 12, simulations of the Zn II λ 2062 line for solar, 32% solar, and 10% solar metallicities ($[\text{Zn}/\text{H}] = 0.0, -0.5, \text{ and } -1.0$), assuming the best-fit b and v values, $b = 15.0 \text{ km s}^{-1}$ and $v = 8.7 \text{ km s}^{-1}$. The parameters of the Cr II λ 2062 line are held fixed in these simulations. These simulations support the profile fitting results that the metallicity appears to be low.

Our results are summarized in Table 9. The errorbars on the abundance estimates include photon noise and the uncertainties in b value, central velocity, and continuum placement. The $[\text{Zn}/\text{H}]$ value for the DLA in Q0827+243 is not well constrained because of the very low SNR in the spectrum of this quasar. The $[\text{Zn}/\text{H}]$ values appear to be low for the DLAs toward Q0738+313 and Q0952+179.

4. The Metallicity-Redshift Relation for DLAs

To examine the implications of our data for the mean metallicity-redshift relation of DLAs, we combined our data with other Zn measurements at higher redshifts. While doing this, we included only the “classical DLAs”, i.e., systems with $\log N_{\text{HI}} \gtrsim 20.3$. Furthermore, we excluded systems with radial velocities within 3000 km s^{-1} from the quasar emission redshifts, since these associated systems may not have similar abundances to those of the intervening systems at the same redshifts. The combined sample contains a total of 87 DLAs with Zn detections or limits, in the redshift range $0.09 < z < 3.90$, and is summarized in Table 10. The sample includes our *HST* data, MMT data for 4 intermediate redshift DLAs recently obtained by us (Khare et al. 2004), and other data from the literature, as detailed in Table 10. While combining these measurements from different studies, we have normalized

them all to the same set of oscillator strengths and solar abundances that we have used for our *HST* data. Our *HST* observations have provided 3 new Zn measurements at $z < 0.39$ where no data existed before. This sample, together with our recent data at $0.6 < z < 1.5$ (Khare et al. 2004), has doubled the $z < 1.5$ sample and increased the $z < 1$ sample by a factor of 2.5. Most of the other recent observations have increased the samples at $z \gtrsim 2$.

We now examine the evolution of the global Zn metallicity for these 87 DLAs. Of these 87 systems, 51 are detections and 36 are limits. One way to deal with the limits is to consider that the true Zn column density for a system with a limit is somewhere between zero and the upper limit value. With this in mind, we first constructed two extreme samples, a “maximum-limits” sample, where we treated the Zn limits as detections, and a “minimum-limits” sample where we treated the Zn limits as zeros. For any individual system, these cases cover the full range of possible values the Zn column densities can take. For the sake of pictorial illustration, we divided each of these samples into six redshift bins with 14 or 15 absorbers each. Figure 13 shows the logarithm of the $N(\text{H I})$ -weighted mean metallicity relative to the solar value for these six bins, plotted as a function of redshift. Each point is plotted at the median redshift in its bin. Horizontal bars for each bin extend from the lowest DLA redshift to the highest DLA redshift within that bin. The top panel shows the “maximum-limits” case. The filled circles in the bottom panel show the “minimum-limits” case with limits treated as zeros. The vertical error bars in both panels show the 1σ uncertainties in the N_{HI} -weighted mean metallicities, and include both the measurement uncertainty in the individual Zn II and H I column density measurements, and the sampling uncertainty. Further descriptions of the statistical procedures can be found in Kulkarni & Fall (2002). Clearly, Fig. 13 shows that the N_{HI} -weighted mean metallicity of DLAs does not rise fast enough to reach solar or near-solar metallicities at $z = 0$.

The above approach is perfectly adequate for low redshifts, which is the main redshift range of interest for our paper, since the number of Zn limits is relatively small at low redshifts. However, at high redshifts, there are a large number of Zn limits. At the same time, for most high- z systems with Zn limits, measurements of other elements are available. We therefore examined how much the results of the “minimum-limits” sample would change if we use information available from other elements for the systems with Zn limits. To do this, we created a third sample, using conservative constraints on the metallicities implied by the information for the other elements (detections or lower limits) available in the literature (Lu et al. 1996; Ledoux et al. 1998; Ledoux, Bergeron, & Petitjean 2002; Prochaska & Wolfe 1999; Prochaska et al. 2001a; 2002; 2003a; 2003b; 2003c; and references therein). For 23 of the 36 systems with Zn upper limits, we estimated lower limits for Zn using measurements of the weakly depleted element Si, and assuming the total (gas + solid phase) relative abundance Si/Zn to be in solar proportion. For one system, we set the Zn abundance

to the abundance of the undepleted element S, assuming solar S/Zn ratio. For most of the remaining systems without Si, S, or O measurements, we set the constraints on Zn using measurements of Fe (8 systems) or Cr (2 systems). While setting the Zn constraints using Fe or Cr, we conservatively added 0.4 dex to correct for a typical amount of depletion in DLAs, unless other elements suggested no depletion. Finally, for two systems, no other measurements could be used to set a lower limit on Zn. In these cases we set the lower limits on Zn abundances to 0.01 solar values, since DLA metallicities are seldom found to be below 0.01 solar. The unfilled circles in the bottom panel of Fig. 13 show the mean metallicity in each redshift bin for this modified minimum-limits sample with the information on other elements used in cases of Zn limits. The two bins at $z > 2.8$ show some change as a result of using the other elements, but there is very little or no change in the other four bins at $z \lesssim 2.8$. Thus our conclusion about the low mean metallicity at low redshifts is not sensitive to whether or not information from other elements is used in cases of Zn limits.

We now quantify the shape of the metallicity-redshift relation using several statistical tests outlined in Kulkarni & Fall (2002). Table 11 lists the results for the binned metallicity-redshift relation for the three samples considered above, in columns 4, 5, and 6. The logarithm of the N_{HI} -weighted mean metallicity in the lowest redshift bin $0.09 < z < 1.37$ is -0.86 ± 0.11 for the maximum-limits sample, -1.01 ± 0.14 for the minimum-limits sample using Zn only (i.e. treating Zn limits as zeros), and -0.93 ± 0.10 for the minimum-limits sample using information from other elements in cases of Zn limits. For the $z < 0.6$ range not accessible to ground-based telescopes, the logarithm of the N_{HI} -weighted mean metallicity is -0.78 for the maximum-limits sample and -0.99 for the minimum-limits sample using information from other elements in cases of Zn limits.

We next fit the data with a straight line relation of the form $\log(\bar{Z}/Z_{\odot}) = \log(\bar{Z}_0/Z_{\odot}) + Bz$, and list the results for the parameters in Table 12. For the binned data (with six bins in the range $0.09 < z < 3.90$), the linear regression slope B of the logarithm of the metallicity vs. redshift relation is -0.18 ± 0.06 for the maximum-limits sample, -0.22 ± 0.08 for the minimum-limits sample with Zn only (i.e. with Zn limits treated as zeros), and -0.23 ± 0.06 for the minimum-limits sample using constraints from other elements in cases of Zn limits. The linear regression intercept of the metallicity-redshift relation (which corresponds to predicted present-day metallicity) is -0.74 ± 0.15 for the maximum-limits sample, -0.75 ± 0.18 for the minimum-limits sample with Zn only, and -0.71 ± 0.13 for the minimum-limits sample using constraints from other elements in cases of Zn limits. Of course, as mentioned by Kulkarni & Fall (2002; see their footnote 3), unlike the means in individual bins, the slopes and intercepts thus determined do not necessarily bracket the true ranges of the slope and the intercept. This is because, in principle, all the true values in cases of upper limits could be closer to the limits at high redshifts, and closer to zero at low redshifts. Nevertheless, these cases are

indicative of the ranges the slope and the intercept are likely to take.

Another approximate, although not rigorously justified, way to get an indication of the slope and intercept of the metallicity-redshift relation from our maximum and minimum limits cases is to take the mean of the logarithmic metallicity estimates for the maximum limits and minimum limits cases in each redshift bin. Column (7) of Table 11 lists the means of the logarithmic metallicity estimates for the maximum limits case (column 4) and the minimum limits case with information from other elements in cases of Zn limits (column 6). The error bars on these mean values include the uncertainty in the values for the maximum and minimum limits cases and the standard deviation of these two values with respect to their mean value. The error bar on the mean value is large for the highest redshift bin ($3.28 < z < 3.90$), which contains mostly limits. The linear regression slope and intercept of the global metallicity-redshift relation obtained on using these mean logarithmic metallicity estimates in each bin are -0.20 ± 0.07 and -0.72 ± 0.16 , respectively.

We have also repeated several other calculations of the metallicity-redshift relation excluding the highest redshift bin (where there are mostly limits rather than detections of Zn); using an unbinned $N(\text{HI})$ -weighted nonlinear χ^2 approach; or using survival analysis, following the methodology of Kulkarni & Fall (2002). In the survival analysis calculations, we computed the Kaplan-Meier (K-M) estimator, using the astronomical survival analysis package ASURV rev. 1.2 (Isobe & Feigelson 1990) which implements the methods of Feigelson & Nelson (1985). The error bars on the survival analysis estimates include the sampling and measurement uncertainties in the column densities. The results of all these calculations are listed in Tables 11 and 12.

Finally, to assess the implications of our *HST* data alone for the statistics of the metallicity-redshift relation, we also repeated our analysis for the 83 systems left after taking out the other new data used here for 4 intermediate-redshift systems from Khare et al. (2004). These calculations yielded essentially identical estimates of the metallicity-redshift relation. For example, for the maximum-limits sample, the N_{HI} -weighted mean metallicity in the lowest redshift bin changes by only ≈ 0.03 dex. The intercept and slope of the metallicity-redshift relation also change by only $\lesssim 0.03$.

The various tests described above give slightly different values, but they all confirm that the slope of the metallicity-redshift relation is small, but probably not zero, and the intercept is low. In other words, the global metallicity of DLAs does not seem to rise to the solar value at low redshifts. This just confirms the visual impression from Fig. 13.

Our estimates of the metallicity-redshift relation are consistent with previous results of Kulkarni & Fall (2002) and Prochaska et al. (2003b). We have not included metallicity

estimates based on X-ray absorption in our analysis here because the X-ray data are expected to reflect mainly the abundance of O, and there could be a systematic difference between $[\text{Zn}/\text{H}]$ and the $[\text{X}/\text{H}]$ derived from the X-ray absorption data.²

To summarize, our analysis suggests that the global metallicity of DLAs stays low at low redshifts, and evolves slowly at most. We stress, however, that the current samples are still small, and further observations, particularly at the low and intermediate redshifts are necessary to decrease the uncertainties in the shape of the metallicity-redshift relation.

We now compare our results with some models of cosmic chemical evolution. The short-dashed, long-dashed, solid, and short-dash-long-dashed curves in Figure 13 show, respectively, (a) the mean interstellar metallicity in the closed-box and outflow models of Pei & Fall (1995); (b) the mean Zn metallicity in the Malaney & Chaboyer (1996) model with a constant Zn yield, a slope of -1.70 for the initial mass function (IMF), and the evolution of the neutral gas density as computed by Pei & Fall (1995); (c) the mean interstellar metallicity in the Pei et al. (1999) model with the optimum fit for the cosmic infrared background intensity; and (d) the mean metallicity of cold interstellar gas in the semi-analytic model of Somerville et al. (2001). Models (a) and (c) agree with the data at high redshifts, but evolve too rapidly toward solar metallicity to be consistent with the data at low redshifts. Models (b) and (d) have lower slopes but predict too high a metallicity at all redshifts. None of the models agrees completely with all the observations.

5. Discussion

The main new result from our study is that, in all the 3 DLAs for which our observations offer meaningful constraints on $[\text{Zn}/\text{H}]$, the metallicities appear to be substantially sub-solar, and that there is at most only a weak evolution in the global mean metallicity with redshift. To understand this puzzling result, we now explore (a) whether our results are affected in any way by the use of Zn as a metallicity indicator, and (b) how our results fit in with

²Prochaska et al. (2003b) reported a slope of -0.25 ± 0.07 for the metallicity-redshift relation in the redshift range $0.5 < z < 4.7.$, a detection of evolution in the global mean metallicity at $\gtrsim 3\sigma$ level. Their analysis included the X-ray measurement from Junkkarinen et al. (2004) for the $z = 0.52$ DLA toward Q0235+164. This system, because of its low redshift and very high H I column density ($\log N_{\text{HI}} = 21.80$), has a very strong influence on the mean metallicity in the lowest redshift bin, and therefore on the overall slope of the mean metallicity-redshift relation. When Kulkarni & Fall (2002) included X-ray absorbers in their analysis, they also found evolution at $\gtrsim 3\sigma$ level (see their footnote 4). For most of their analysis, Kulkarni & Fall (2002) left out X-ray absorbers since the X-ray measurements primarily trace the O abundance, which could differ systematically from the Zn abundance.

the morphological information available for these DLAs. Finally, we discuss the role of potential selection effects caused by dust obscuration in the DLAs.

5.1. Zinc as the Metallicity Indicator

Could the apparent low metallicity for most of our target DLAs be an artifact of the use of Zn as the metallicity indicator? To explore this question, we now examine the advantages and disadvantages of using Zn.

The conclusion that $[Zn/Fe] \sim 0$ in Galactic halo and disk stars for metallicities $[Fe/H] \gtrsim -3$ that followed from earlier work (Snedden, Gratton, & Crocker 1991) has been strongly supported by recent studies (e.g., Mishenina et al. 2002; Cayrel et al. 2004; Nissen et al. 2004). There is some evidence for a small overabundance of Zn by $\sim 0.1 - 0.2$ dex in metal-poor disk stars and halo stars with $[Fe/H] < -2$ (e.g., Prochaska et al. 2000; Bihain et al. 2004; Cayrel et al. 2004). Chen et al. (2004) have also recently reported $[Zn/Fe] \sim 0.1 - 0.15$ dex in disk stars with $[Fe/H] > -0.9$. However, in all of these studies, there are systematic uncertainties in $[Zn/Fe]$ at the level of $\approx \pm 0.1$ dex, and overall Zn tracks Fe quite closely for $[Fe/H] > -2$. These observations are not completely understood in nucleosynthetic models of massive stars. The models are complex and the value of $[Zn/Fe]$ depends on several parameters such as the position of the mass cut, the explosion energy, the degree of neutronization, and the consequences of a neutrino-driven wind (Woosley & Weaver 1995; Chieffi & Limongi 2002; Umeda & Nomoto 2002; Woosley, Heger, & Weaver 2002; Fenner, Prochaska, & Gibson 2004). Despite these uncertainties in the theoretical understanding, the Galactic stellar data support the use of Zn as a tracer of metallicity.

There are some observational difficulties in measuring the Zn abundances in DLAs. The Zn II $\lambda\lambda 2026, 2062$ lines are weak and sometimes hard to detect. On the other hand, for that same reason, they are usually unsaturated. At $z \gtrsim 3$, the Zn II lines lie in spectral regions affected by night sky lines, and thus become difficult to detect. At the same time, the long wavelengths of the Zn II lines also make them accessible in near-UV and optical spectra for the range $z \lesssim 3$ which spans $\approx 90\%$ of the cosmic history.

While some studies have suggested that ionization corrections for Zn could be significant (e.g., Howk & Sembach 1999), others have given convincing arguments that such corrections are negligible. For example, Vladilo et al. (2001) have pointed out that the ionization corrections are uncertain because of uncertainties in the Zn recombination coefficients and ionization cross sections. They have provided evidence that the Zn ionization corrections could be lower, and concluded that DLA metallicity estimates based on $[Zn/H]$ are unlikely

to be significantly affected by ionization effects. Indeed, at the large H I column densities ($\log N_{\text{HI}} = 20.9 - 21.3$) of the 3 DLAs in our sample where we find low $[\text{Zn}/\text{H}]$, the ionization correction for $[\text{Zn}/\text{H}]$ is expected to be at most about 0.3 dex, and probably smaller for more accurate atomic parameters (see, e. g., Fig. 16 of Vladilo et al. 2001).

Thus, while Zn, like all other elements, has both advantages and disadvantages, it is still an appropriate choice as a metallicity indicator in DLAs (see, e.g., Bihain et al. 2004; Nissen et al. 2004). Furthermore, the various uncertainties mentioned above are not large enough to make significant difference to our results regarding a low global mean metallicity (≈ -0.7 to -1.0 dex) at low redshifts. Overall, we conclude that our main result is not affected much by the use of Zn as the primary metallicity indicator.

5.2. Comparison with Morphological Information

Could the low metallicities in our low-redshift DLAs be understood in terms of the nature of the underlying galaxies? In fact, the low metallicities are consistent with the morphological information available on the candidate galaxies believed to give rise to these DLAs.

The $z = 0.0912$ DLA toward Q0738+313 has been tentatively identified as associated with fuzz surrounding the quasar, and classified as a low surface brightness galaxy. This galaxy has an estimated luminosity of $0.08L_K^*$ and impact parameter $< 3.6 h^{-1}$ kpc for $\Omega_m = 1$, $\Omega_\Lambda = 0$, and $H_0 = 65 h \text{ km s}^{-1} \text{ Mpc}^{-1}$ (Cohen 2001; Turnshek et al. 2001). The $z = 0.2212$ DLA toward the same quasar has been spectroscopically identified as a dwarf spiral galaxy, with B and K-band luminosities of $0.1L_B^*$ and $0.1L_K^*$, respectively, and impact parameter of $20 h^{-1}$ kpc (Cohen 2001; Turnshek et al. 2001).

From ground-based images in the B, R, J, and K bands, Rao et al. (2003) have suggested that the best candidates for the $z = 0.2378$ DLA toward Q0952+179 are two dwarf low surface brightness galaxies with a combined luminosity of $0.02L_K^*$, and impact parameter $< 4.5 h^{-1}$ kpc. However, these candidate objects have not yet been confirmed spectroscopically. In any case, the DLA in this field cannot be an L^* galaxy, as none of the luminous galaxies in the field have the same redshift as the DLA (Bergeron & Boissé 1991).

For Q0827+243 ($z_{\text{abs}} = 0.5247$), where we have only a loose upper limit on the metallicity, a galaxy at $z = 0.5258$ has been spectroscopically confirmed at an angular separation of $6''$, corresponding to a projected separation of $34 h^{-1}$ kpc. This galaxy has B and K-band luminosities of $0.8L_B^*$ and $1.2L_K^*$, respectively. Rao et al. (2003) have suggested a “disturbed spiral” morphology for this galaxy. Unfortunately, our Zn data do not yield a firm deter-

mination of the metallicity in this DLA. The Fe abundance is low ($[\text{Fe}/\text{H}] = -1.02 \pm 0.05$; Khare et al. 2004); but this could be partly because of depletion of Fe on dust grains, and the total (gas + solid phase) metallicity could be higher. In any case, at the large impact parameter for this absorber, the metallicity is likely to be low, for a typical abundance gradient of $\sim 0.05 - 0.1$ dex kpc^{-1} observed in the Milky Way (e.g., Friel & Janes 1993).

5.3. Potential Selection Effects

Our observations of low metallicities in low-redshift DLAs are surprising because the mean mass-weighted interstellar metallicity of nearby galaxies is found to be close to solar (e.g., Kulkarni & Fall 2002). Thus, samples derived from absorption-line studies of optically selected quasars seem to be biased toward less metal-rich galaxies than would be expected from an H I emission-selected sample of galaxies.

The low metallicities of our low- z DLAs also appear to contradict the expectations of a solar or near-solar metallicity at $z = 0$ from most cosmic chemical evolution models based on the global star formation history of galaxies. Our observations thus suggest that the current DLA samples, especially those at low redshifts, might not be representative of the global galaxy population. If the observed DLAs have low metallicities at all redshifts, it is possible that the DLA galaxies are dominated by dwarf or low surface brightness galaxies. Some earlier studies have suggested that DLAs could arise in dwarf galaxies (e.g., York et al. 1986, Matteucci et al. 1997). Indeed, some imaging studies have suggested DLAs at low redshifts to be predominantly dwarf or low surface brightness galaxies (e.g., Rao et al. 2003). In fact, as discussed in section 5.2, three out of the four DLAs in our sample are tentatively identified as dwarf or low surface brightness galaxies (although only one of them is spectroscopically confirmed). Again, taken at face value, this is very surprising because the H I emission studies of galaxies at $z = 0$ show that most of the H I at the present epoch resides in large spirals (e.g., Rao & Briggs 1993; Zwaan, Briggs, & Sprayberry 2001). Of course, the identification of low- z DLAs with dwarf or low surface brightness galaxies is not always certain, since many imaging studies (e.g., LeBrun et al. 1997; Rao et al. 2003) have not always confirmed the redshifts of the candidate galaxies. Chen & Lanzetta (2003) have obtained more extensive photometric redshift data for DLA fields and suggested that the contribution of dwarf galaxies to DLAs at $z < 1$ is not significant. Rosenberg & Schneider (2003) have also suggested that the luminosity function of low-redshift DLAs may be fairly flat over several orders of magnitude. Thus, there seems to be no full consensus about the nature of low-redshift DLAs. Clearly, it is necessary to obtain further imaging studies and redshift identifications of low-redshift DLAs and take into account the luminosity

uncertainties of the DLA galaxies.

Our observations of low metallicities in low-redshift DLAs suggest that these galaxies have had less nucleosynthetic processing and hence low time-averaged star formation rates (SFRs). On the other hand, observations of the UV luminosity density of galaxies (e.g. Lilly et al. 1996; Madau et al. 1996) indicate that the global average SFR in galaxies was high at $z \gtrsim 1.5$. In fact, it is this high global SFR at high redshifts that drives the metallicity to rise up to solar or near-solar levels by the present epoch in most cosmic chemical evolution models. There are also indications from C II* absorption that some DLAs may have high SFRs and could be efficient producers of heavy elements (e.g., Wolfe et al. 2003). If the observed low-redshift DLAs are largely metal-poor, then where are the more metal-rich low- z absorbers expected to have near-solar metallicities? Why are the absorption studies not detecting more luminous and metal-rich DLAs even at low redshifts? Such a selection effect could be caused by dust obscuration in the DLAs. This is because the DLA galaxies with the highest column densities of metals are likely to be those with the highest column densities of dust, and these may obscure background quasars to such a degree that some of them are omitted from optically selected samples (Fall & Pei 1993; Boisse et al. 1998). As a result of obscuration, the observed mean metallicity in the DLA galaxies, and hence the data points in Figure 13, could lie systematically below the true mean metallicity. The model predictions plotted in Fig. 13, however, refer to the “true” mean metallicity (not corrected for dust obscuration). Indeed, if the true mean metallicity and dust content increase with decreasing redshift, more DLAs could be missing at lower redshifts. This would flatten the metallicity-redshift relation, as possibly shown by our observations.

In principle, a comparison of metal abundances in DLAs from optical vs. radio-selected quasars can help to quantify the dust selection effect. At high redshifts, Ellison et al. (2001) found slightly more DLAs in the foreground of radio-selected and optically faint quasars than in optically selected and optically bright quasars. This result is sometimes misinterpreted as evidence against dust selection effects. However, the radio-selected samples are still small, and the uncertainties correspondingly large. The difference between the true (unobscured) and observed column density distributions $f(N_{\text{HI}})$ of DLAs is expected to be only $\lesssim 50\%$ for $\log N_{\text{HI}} < 21$ (see Fig. 1 of Pei & Fall 1995). The Ellison et al. (2001) points, within the error bars, are in fact consistent with the predictions of Fall & Pei (1993), Pei & Fall (1995), and Pei et al. (1999). Recent results of Ellison et al. (2004) for Mg II systems with $0.6 < z < 1.7$ also appear to be consistent, within the large error bars, with the predictions of Fall & Pei (1993), Pei & Fall (1995), and Pei et al. (1999), although exact comparisons of $f(N_{\text{HI}})$ of DLAs can only be made after the DLA nature of the Mg II systems is confirmed with UV spectra. In a study of reddening in quasars with and without DLAs, Murphy & Liske (2004) have recently suggested that the extent of dust reddening caused by high-redshift DLAs may

be small at $z \sim 3$, but the effects at low redshift are likely to be larger. Indeed, Vladilo (2004) has reported that the dust-to-metals ratio in DLAs, as inferred from the depletion of Fe, increases with decreasing redshift. Abundance studies for a very large sample of DLAs in radio-selected and optically faint quasars would help to improve the constraints on the extent of the dust obscuration bias.

6. Summary

We have obtained *HST* STIS UV spectra of three quasars with four DLAs in the redshift range $0.09 < z < 0.52$, to constrain the abundances of Zn, Cr, and Fe in these absorbers. These observations have provided the first constraints on Zn abundances in DLAs with $z < 0.4$. In all the 3 DLAs for which our observations offer meaningful constraints on the Zn abundance, the metallicities appear to be substantially sub-solar ($\lesssim 10 - 20\%$ solar). We have combined our results with higher redshift data from the literature to estimate the global mean metallicity-redshift relation for DLAs. We find that the global mean metallicity of DLAs shows at most a slow increase with decreasing redshift and does not appear to rise up to solar or near-solar values at $z = 0$. On the other hand, most cosmic chemical evolution models, based on the global star formation history inferred from the emission studies of galaxies, predict the global interstellar metallicity to be solar or near-solar at $z = 0$. This suggests that the DLAs, especially those at low redshifts, do not trace the general population of galaxies represented by the global star formation history of the universe. The low $N(\text{H I})$ -weighted mean metallicity of low-redshift absorbers also appears to contradict the fact that the mass-weighted mean interstellar metallicity of nearby galaxies is observed to be close to solar.

This weak evolution in the DLA global mean metallicity could be explained by the fact that our sample seems to be dominated by dwarf or low surface brightness galaxies. It is possible that current DLA samples, especially those at low redshifts, are biased against more enriched galaxies because the latter may cause more dust obscuration of the background quasars. We note, however, that the low-redshift samples are still small, and the fact that most of the DLAs in our sample are metal-poor could be an effect of small number statistics. Metallicity measurements of more low-redshift DLAs are necessary to further improve the statistics of the mean metallicity-redshift relation and to study the scatter around the mean. Observations of low-redshift DLAs toward optically faint quasars are especially necessary in the future to improve the constraints on the mean metallicity-redshift relation for DLAs, and to quantify potential dust selection effects.

VPK, SMF, and JTL acknowledge partial support from the NASA / Space Telescope Science Institute grant GO-9441. VPK also acknowledges partial support from the National Science Foundation grant AST-0206197. DEW acknowledges support from the NASA LTSA grant NAG5-11413. JWT acknowledges support of the NSF Physics Frontier Center, Joint Institute for Nuclear Astrophysics under grant PHY 02-16783 and DOE support under grant DE-FG 02-91ER 40606. We thank Drs. Steven Beckwith, Bahram Mobasher, Charles Proffitt and Anthony Roman of STScI for help with execution and calibration of our STIS observations. We also thank J. Meiring for assistance with data analysis. Finally, we thank an anonymous referee for helpful comments on the paper.

Facilities: HST(STIS).

REFERENCES

- Bergeron, J. & Boissé P. 1991, *A&A*, 243, 344
- Bergeson, S. D., & Lawler, J. E. 1993, *ApJ*, 408, 382
- Bergeson, S. D., Mullman, K. L., & Lawler, J. E. 1994, *ApJ*, 435, 157
- Bihain, G., Israelian, G., Rebolo, R., Bonifacio, P., & Molaro, P. 2004, *A&A*, in press (astro-ph/0405050)
- Boissé, P., Le Brun, V., Bergeron, J. & Deharveng, J.-M. 1998, *A&A*, 333, 841
- Cayrel, R. et al. 2004, *A&A*, 416, 1117
- Centurión, M., Molaro, P., Vladilo, G., Peroux, C., Levshakov, S. A., & D’Odorico, V 2003, *A&A*, 403, 55
- Chen, H.-W., & Lanzetta, K. M. 2003, *ApJ*, 597, 706
- Chen, Y. Q., Nissen, P. E., & Zhao, G. 2004, *A&A*, submitted (astro-ph/0406612)
- Chengalur, J. N., & Kanekar, N. 1999, *MNRAS*, 302, L29
- Chieffi, A., & Limongi, M. 2002, *ApJ*, 557, 281
- Cohen, J. G. 2001, *AJ*, 121, 1275
- de la Varga, A., Reimers, D., Tytler, D., Barlow, T., & Burles, S. 2000, *A&A*, 363, 69

- Dessauges-Zavadsky, M., Proux, C., Kim, T.-S., D’Odorico, S., & McMahon, R. G. 2003, MNRAS, 345, 447
- Dessauges-Zavadsky, M., Calura, F., Prochaska, J. X., D’Odorico, S., & Matteucci, F. 2004, A&A, 416, 79
- Ellison, S. L., Churchill, C. W., Rix, S. A., & Pettini, M. 2004, ApJ, in press (astro-ph/0407237)
- Ellison, S. L. & Lopez, S. 2001, A&A, 380, 117
- Ellison, S. L. Yan, L., Hook, I. M., Pettini, M., Wall, J. V., & Shaver, P. 2001, A&A, 379, 393
- Fall, S. M., & Pei, Y. C. 1993, ApJ, 402, 479
- Feigelson, E. D. & Nelson, P. I. 1985, ApJ, 293, 192
- Fenner, Y., Prochaska, J. X., & Gibson, B. K. 2004, ApJ, 606, 116
- Friel, E. D., & Janes, K. A. 1993, A&A, 267, 75
- Ge, J., Bechtold, J., & Kulkarni, V. P. 2001, ApJ, 547, L1
- Howk, J. C., & Sembach, K. R. 1999, ApJ, 523, L141
- Isobe, T. & Feigelson, E. D. 1990, BAAS, 22, 917
- Jenkins, E. B. 1986, ApJ, 304, 739
- Junkkarinen, V. T., Cohen, R. D., Beaver, E. A., Burbidge, E. M., Lyons, R. W., & Madejski, G. 2004, ApJ, in press (astro-ph/0407281)
- Kanekar, N., Ghosh, T., & Chengalur, J. N. 2001, A&A, 373, 394
- Kanekar, N., & Chengalur, J. N. 2001, A&A, 369, 42
- Khare, P., Kulkarni, V. P., Lauroesch, J. T., York, D. G., Crotts, A. P. S., & Nakamura, O. 2004, ApJ, in press (astro-ph/0408139)
- Kulkarni, V. P., Huang, K., Green, R. F., Bechtold, J., Welty, D. E., & York, D. G. 1996, MNRAS, 279, 197
- Kulkarni, V. P., Fall, S. M. & Truran, J. W. 1997, ApJ, 484, L7

- Kulkarni, V. P., Bechtold, J., & Ge, J. 1999, in Proc. of ESO Conference on “Chemical Evolution from Zero to High Redshifts”, eds. M. Rosa and J. Walsh, (Springer-Verlag), 275
- Kulkarni, V. P. & Fall, S. M. 2002, ApJ, 580, 732
- Lane, W., Smette, A., Briggs, F., Rao, S., Turnshek D., & Meylan, G. 1998, AJ, 116, 26
- Lanzetta, K. M., Wolfe, A. M., & Turnshek, D. A. 1995, ApJ, 440, 435
- Lebrun, V., Bergeron, J., Boisse, P., & Deharveng, J. M. 1997, A&A, 321, 733
- Ledoux, C., Petitjean, P., Bergeron, J., Wampler, E. J., & Srianand, R. 1998, A&A, 337, 51
- Ledoux, C., Bergeron, J., & Petitjean, P. 2002, A&A, 385, 802
- Ledoux, C., Srianand, R., & Petitjean, P. 2002, A&A, 392, 781
- Ledoux, C., Petitjean, P., & Srianand, R. 2003, MNRAS, 346, 209
- Levshakov, S. A., Agafonova, I. I., Centurin, M., & Mazets, I. E. 2002, A&A, 383, 813
- Lilly, S. J., Le Fevre, O., Hammer, F., & Crampton, D. 1996, ApJ, 460, L1
- Lodders, K. 2003, ApJ, 591, 1220
- Lopez, S., & Ellison, S. L. 2003, A&A, 403, 573
- Lopez, S., Reimers, D., D’Odorico, S., & Prochaska, J. X. 2002, A&A, 385, 778
- Lopez, S., Reimers, D., Rauch, M., Sargent, W. L. W. & Smette, A. 1999, ApJ, 513, 598
- Lu, L., Savage, B. D., Tripp, T. M., & Meyer, D. M. 1995, ApJ, 447, 597
- Lu, L., Sargent, W. L. W., Barlow, T. A., Churchill, C. W., & Vogt, S. S. 1996, ApJS, 107, 475
- Madau, P. et al. 1996, MNRAS, 283, 1388
- Malaney, R. A., & Chaboyer, B. 1996, ApJ, 462, 57
- Matteucci, F. Molaro, P. & Vladilo, G. 1997, A&A, 321, 45
- Meyer, D. M., & York, D. G. 1992, ApJ, 399, L121
- Meyer, D. M., Lanzetta, K. M., & Wolfe, A. M. 1995, ApJ, 451, L13

- Mishenina, T. V., Kovtyukh, V. V., Soubiran, C., Travaglio, C., & Busso, M. 2002, *A&A*, 396, 189
- Molaro, P., Bonifacio, P., Centurion, M., D’Odorico, S., Vladilo, G., Santin, P., & Di Marcantonio, P. 2001, *ApJ*, 541, 5
- Murphy, M. T., & Liske, J. 2004, *MNRAS*, submitted (astro-ph/0405472)
- Nissen, P. E., Chen, Y. Q., Asplund, M., & Pettini, M. 2004, *A&A*, 415, 993
- Pei, Y. C. & Fall, S. M. 1995, *ApJ*, 454, 69
- Pei, Y. C., Fall, S. M., & Hauser, M. G. 1999, *ApJ*, 522, 604
- Peroux, C., Petitjean, P., Aracil, B., & Srianand, R. 2002, *NewA*, 7, 577
- Petitjean, P., Srianand, R., & Ledoux, C. 2000, *A&A*, 364, L26
- Petitjean, P., Srianand, R., & Ledoux, C. 2002, *MNRAS*, 332, 383
- Pettini, M., Smith, L. J., Hunstead, R. W., & King, D. L. 1994, *ApJ*, 426, 79
- Pettini, M., King, D. L., Smith, L. J. & Hunstead, R. W. 1997, *ApJ*, 478, 536
- Pettini, M., Ellison, S. L., Steidel, C. C., & Bowen, D. V. 1999, *ApJ*, 510, 576
- Pettini, M., Ellison, S. L., Steidel, C. C., Shapley, A. E., Bowen, D. V. 2000, *ApJ*, 532, 65
- Prochaska, J. X., & Wolfe, A. M. 1997, *ApJ*, 474, 140
- Prochaska, J. X., & Wolfe, A. M. 1998, *ApJ*, 507, 113
- Prochaska, J. X., & Wolfe, A. M. 1999, *ApJS*, 121, 369
- Prochaska, J. X., Naumov, S. O., Carney, B. W., McWilliam, A., & Wolfe, A. M. 2000, *AJ*, 120, 2513
- Prochaska, J. X., & Wolfe, A. M. 2000, *ApJ*, 533, L5
- Prochaska, J. X. et al. 2001a, *ApJS*, 137, 21
- Prochaska, J. X., Gawiser, E., & Wolfe, A. M. 2001b, *ApJ*, 552, 99
- Prochaska, J. X., Howk, J. C., O’Meara, J. M., Tytler, D., Wolfe, A. M., Kirkman, D., Lubin, D., & Suzuki, N. 2002, *ApJ*, 571, 693

- Prochaska, J. X., Castro, S., & Djorgovski, S. G. 2003a, *ApJS*, 148, 317
- Prochaska, J. X., Gawiser, E., Wolfe, A. M., Castro, S., & Djorgovski, S. G. 2003b, *ApJ*, 595, L9
- Prochaska, J. X., Gawiser, E., Wolfe, A. M., Cooke, J., & Gelino, D. 2003c, *ApJS*, 147, 227
- Rao, S., & Briggs, F. 1993, *ApJ*, 419, 515
- Rao, S. M., & Turnshek, D. A. 1998, *ApJ*, 500, L115
- Rao, S. M., & Turnshek, D. A. 2000, *ApJS*, 130, 1
- Rao, S. M., Nestor, D. B., Turnshek, D. A., Lane, W. M., Monier, E. M., & Bergeron, J. 2003, *ApJ*, 595, 94
- Rao, S. M., Turnshek, D. A., & Nestor D. B. 2004 (in preparation)
- Rosenberg, J. L., & Schneider, S. E. 2003, *ApJ*, 585, 256
- Savage, B. D., & Sembach, K. R. 1991, *ApJ*, 379, 245
- Savaglio, S. 2001, in *The Extragalactic Infrared Background and its Cosmological Implications*, IAU Symposium, 204, ed. M. Harwit and M. G. Hauser, (ASP: San Francisco), 24
- Sembach, K. R., & Savage, B. D. 1992, *ApJS*, 83, 147
- Snedden, C., Gratton, R.G., & Crocker, D.A. 1991, *A&A*, 246, 354
- Somerville, R. S., Primack, J. R., & Faber, S. M. 2001, *MNRAS*, 320, 504
- Tissera, P. B., Lambas, D. G., Mosconi, M. B., & Cora, S. 2001, *ApJ*, 557, 527
- Turnshek D. A., Rao, S., Nestor, D., Lane, W., Monier, E., Bergeron, J., & Smette, A. 2001, *ApJ*, 553, 288
- Umeda, H., & Nomoto, K. 2002, *ApJ*, 565, 385
- Vidal-Madjar, A., Laurent, C., Bonnet, R. M., & York, D. G. 1977, *ApJ*, 211, 91
- Vladilo, G., Bonifacio, P., Centurion, M., & Molaro, P. 2000, *ApJ*, 543, 24
- Vladilo, G., Centurion, M., Bonifacio, P., & Howk, J. C. 2001, *ApJ*, 557, 1007
- Vladilo, G. 2004, *A&A*, in press (astro-ph/0403237)

- Welty, D. E., Hobbs, L. M., & York, D. G. 1991, ApJS, 75, 425
- Wolfe, A. M., Lanzetta, K. M., Foltz, C. B., & Chaffee, F. H. 1995, ApJ, 454, 698
- Wolfe, A. M., Gawiser, E., & Prochaska, J. X. 2003, ApJ, 593,235
- Woosley, S.E., & Weaver, T.A. 1995, ApJS, 101, 181
- Woosley, S.E., Heger, A., & Weaver, T.A. 2002, RvMP, 74, 1015
- York, D. G., Dopita, M., Green, R., & Bechtold, J. 1986, ApJ, 311, 610
- Zwaan, M. A., Briggs, F. H., & Sprayberry, D. 2001, MNRAS, 327, 1249

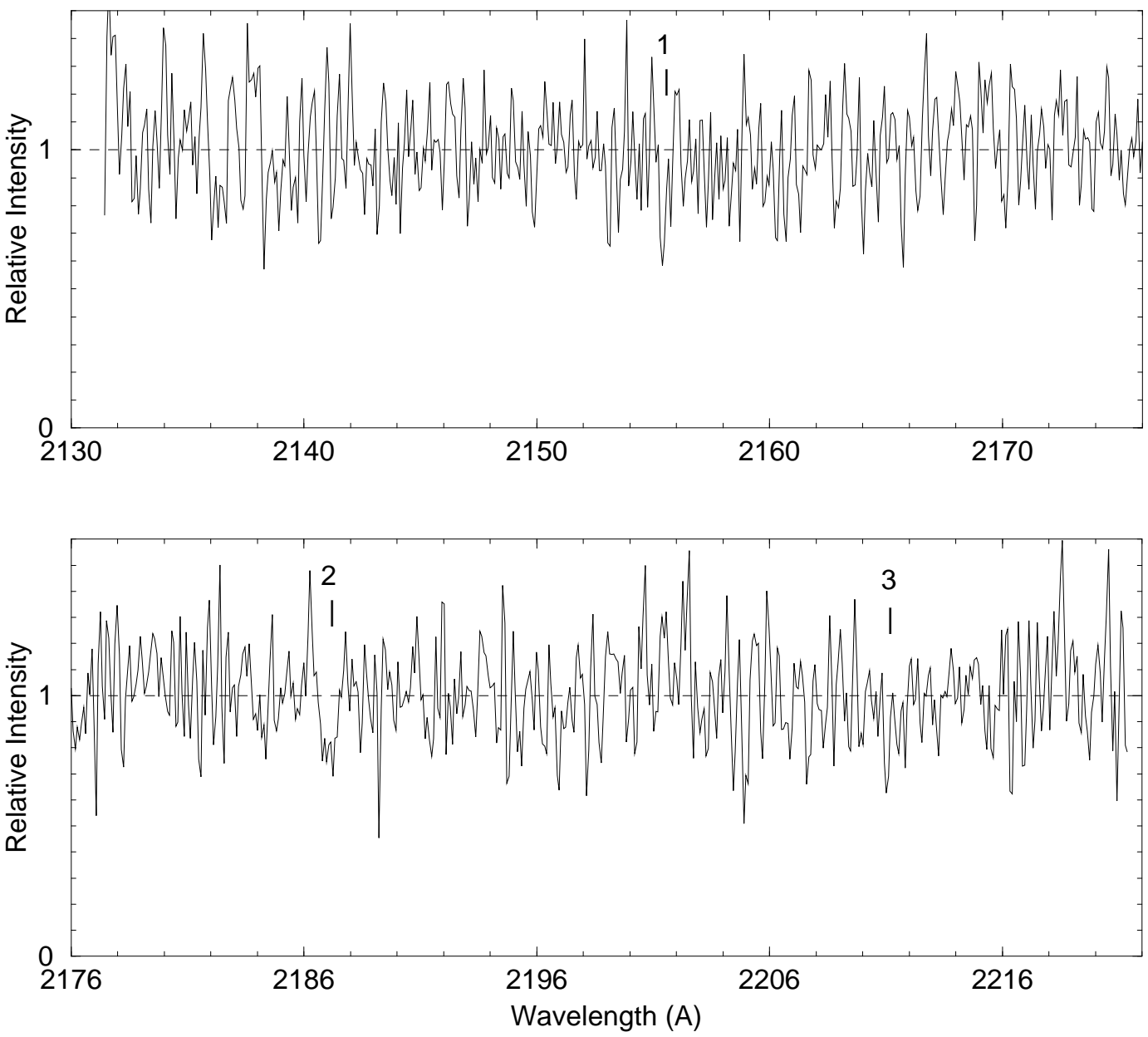


Fig. 1.— HST STIS spectrum of Q0738+313 observed with the G230M grating setting centered at 2176 Å.

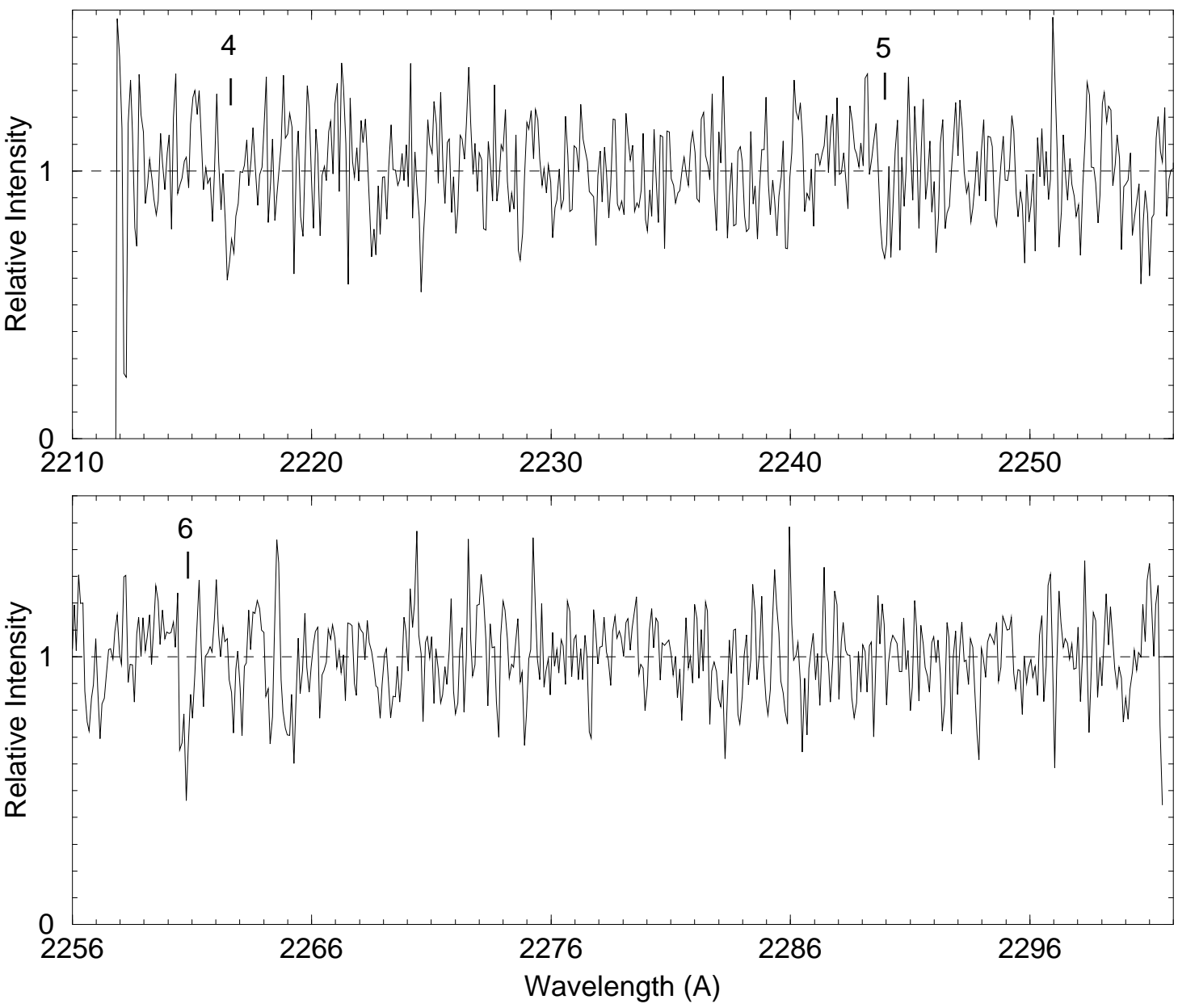


Fig. 2.— HST STIS spectrum of Q0738+313 observed with the G230M grating setting centered at 2257 Å.

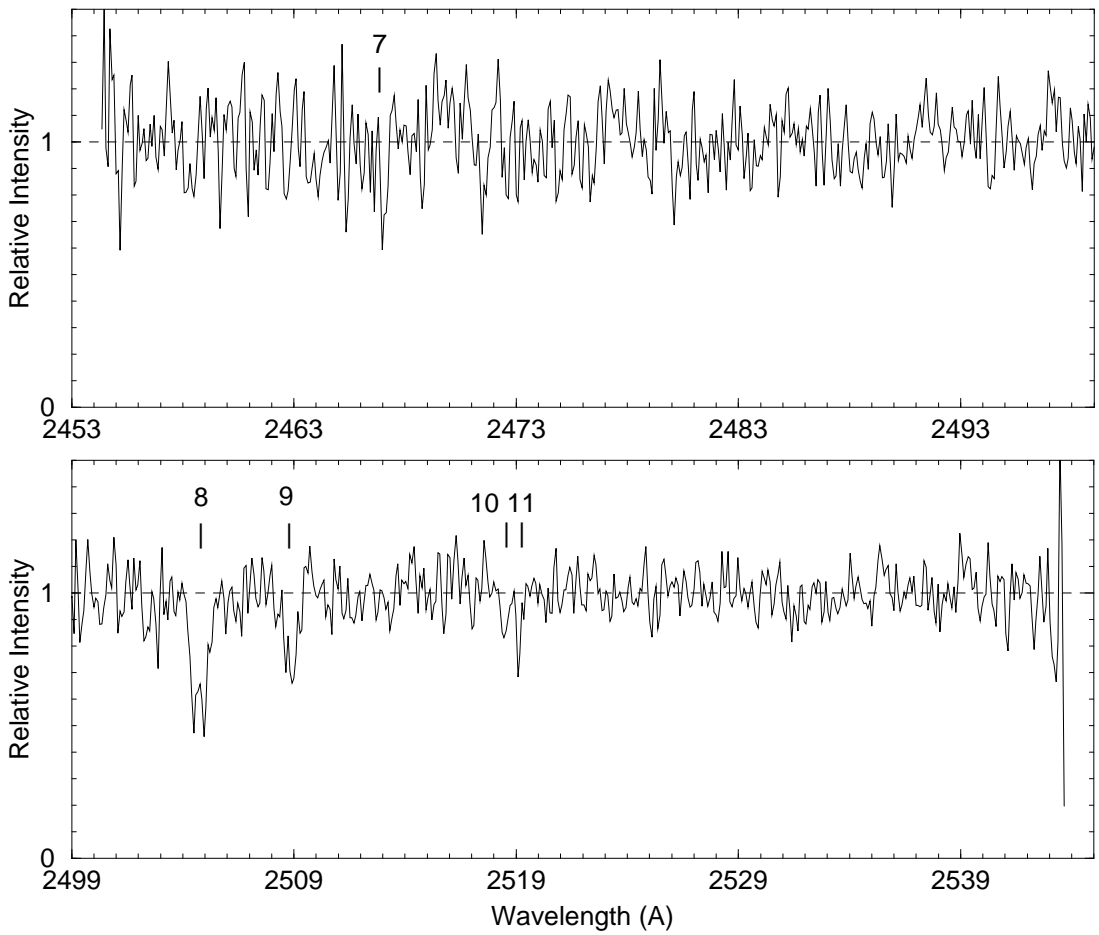


Fig. 3.— HST STIS spectrum of Q0738+313 observed with the G230M grating setting centered at 2499 Å.

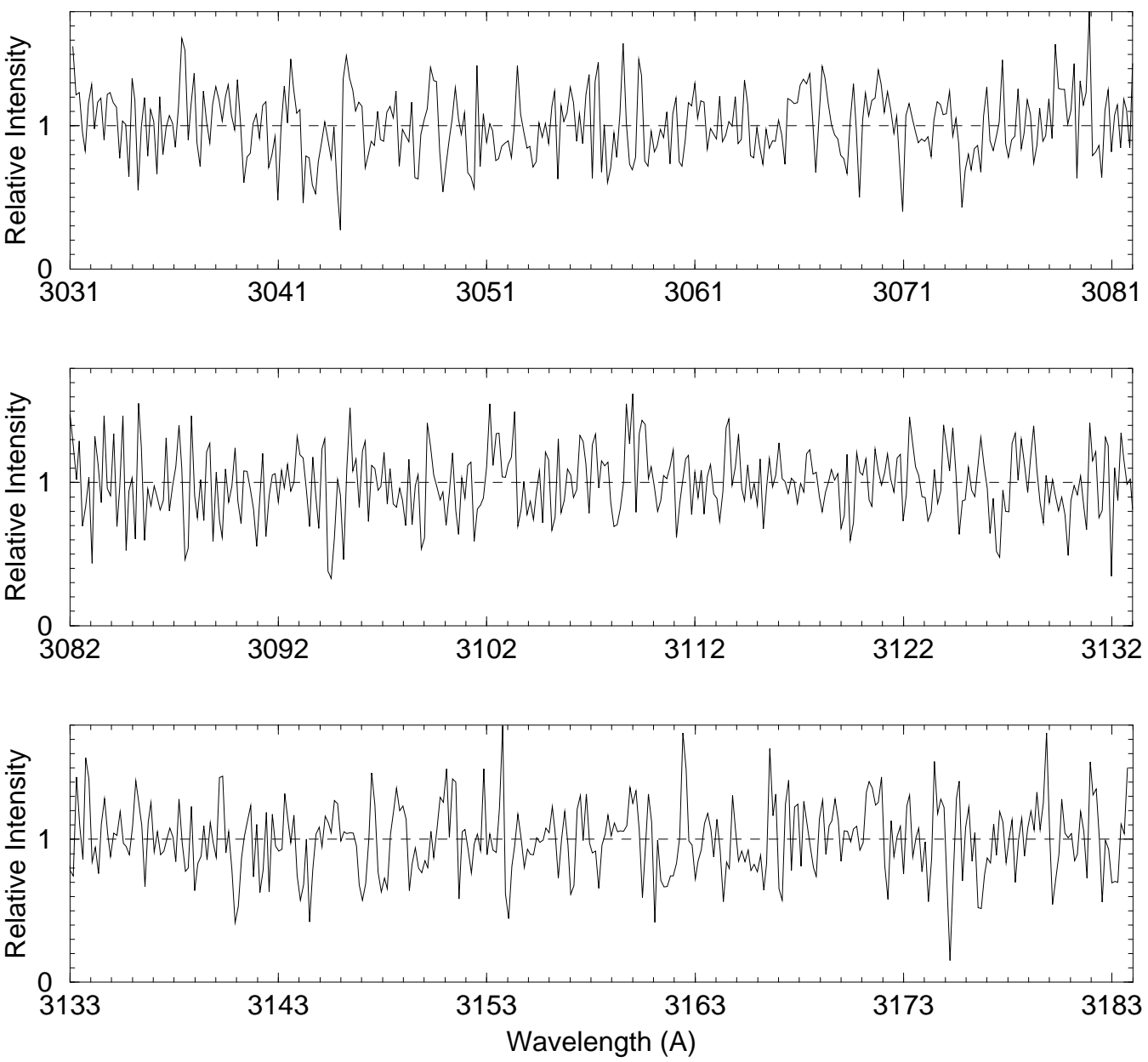


Fig. 4.— HST STIS spectrum of Q0827+243 observed with the G230MB grating setting centered at 3115 Å.

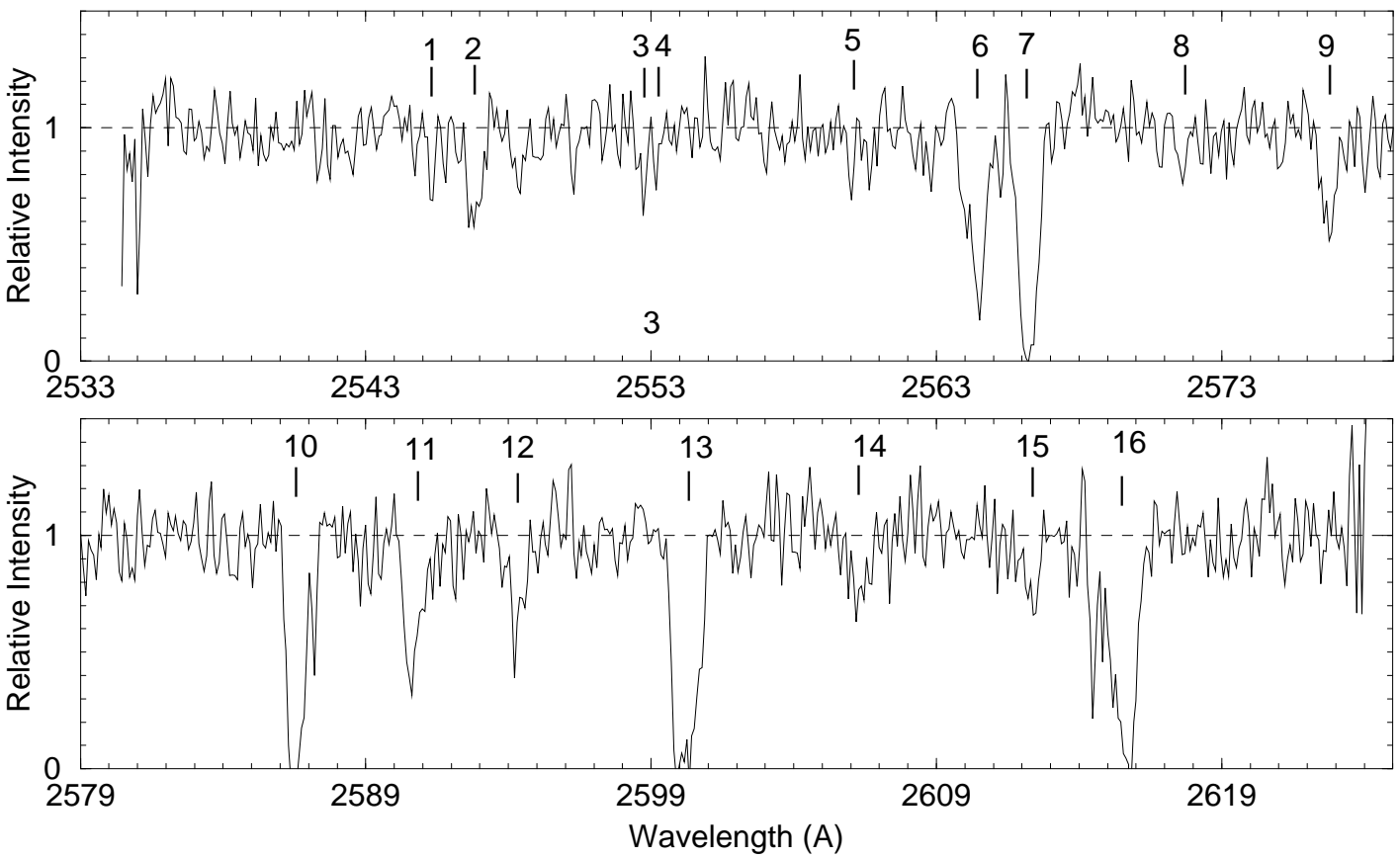


Fig. 5.— HST STIS spectrum of Q0952+179 observed with the G230M grating setting centered at 2579 Å.

Q0738+313 $z_{\text{abs}} = 0.0912$

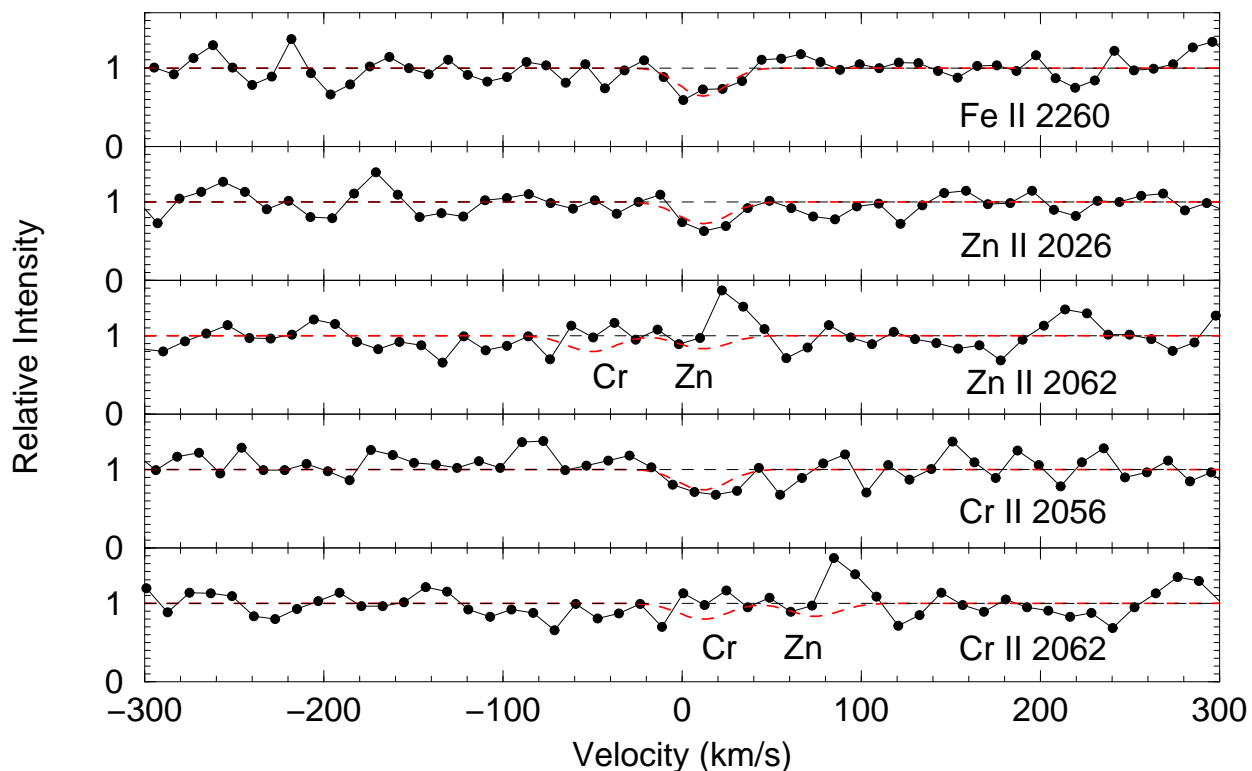


Fig. 6.— Velocity plot of the Fe II, Zn II, and Cr II data for the $z = 0.0912$ DLA toward Q0738+313. The zero point of the velocity scale refers to the absorption redshift $z = 0.0912$ inferred from the 21-cm and optical data. The dashed curves show the profiles for the best-fit N , b , and v parameters obtained by fitting multiple lines simultaneously. In the case of Zn II, the profiles correspond to the 3σ upper limit adopted.

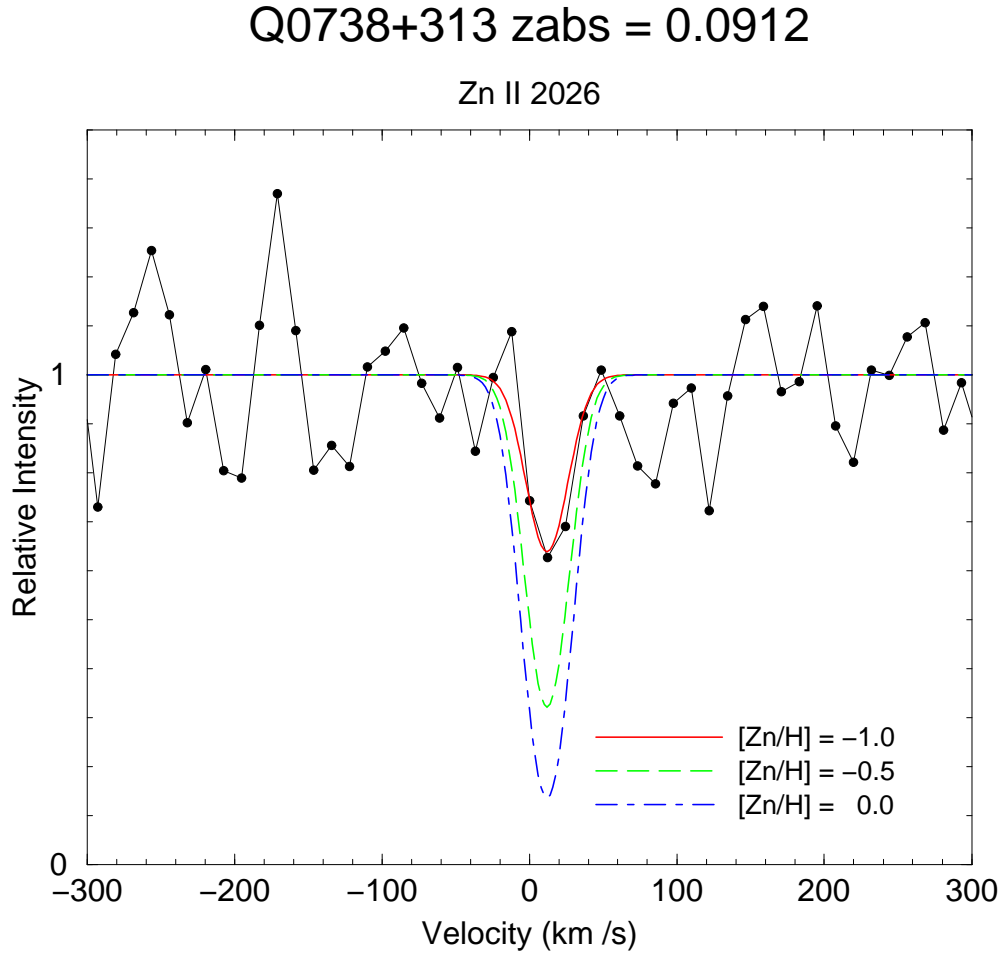


Fig. 7.— Comparison of Zn II $\lambda 2026$ data for the $z = 0.0912$ DLA toward Q0738+313 with simulated Voigt profiles for $[\text{Zn}/\text{H}] = -1.0$, -0.5 , and 0.0 , shown by solid (red), short-dashed (green), and short-dash-long-dashed (blue) curves, respectively. All three curves assume the best-fit b and v values obtained by fitting multiple lines simultaneously.

Q0738+313 $z_{\text{abs}} = 0.2212$

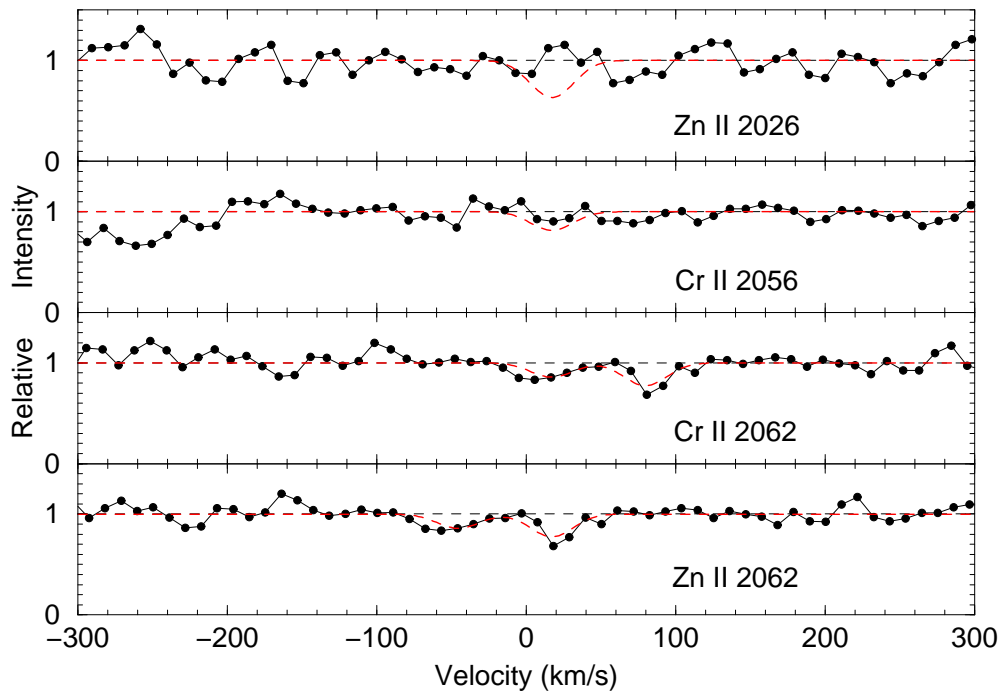


Fig. 8.— Velocity plot of the Zn II and Cr II data for the $z = 0.2212$ DLA toward Q0738+313. The zero point of the velocity scale refers to the absorption redshift $z = 0.2212$ inferred from the 21-cm and optical data. The dashed curves show the profiles for the best-fit N , b , and v parameters obtained by fitting multiple lines simultaneously. In the case of Zn II, the profiles correspond to the 3σ upper limit adopted.

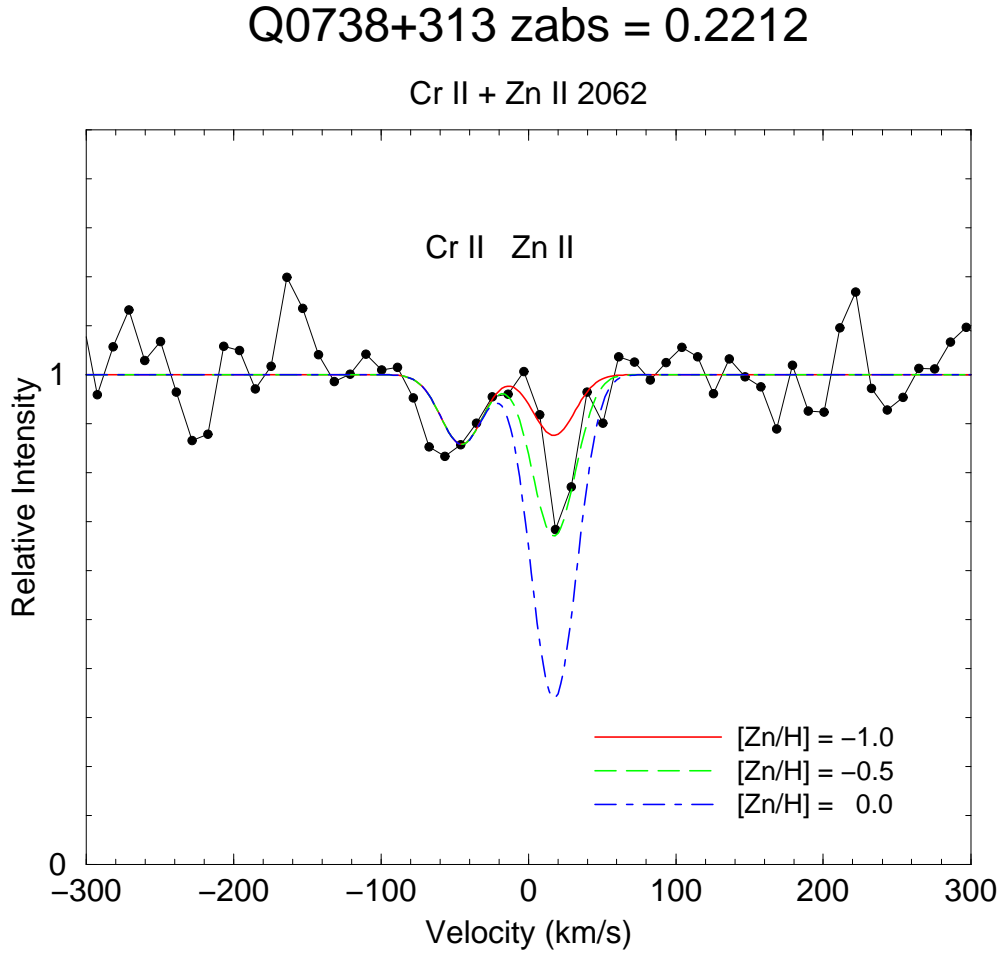


Fig. 9.— Comparison of Zn II $\lambda 2062.664$ data for the $z = 0.2212$ DLA toward Q0738+313 with simulated Voigt profiles for $[\text{Zn}/\text{H}] = -1.0$, -0.5 , and 0.0 , shown by solid (red), short-dashed (green), and short-dash-long-dashed (blue) curves, respectively. All three curves assume the best-fit values of b , v , and Cr II column density obtained by fitting multiple lines simultaneously.

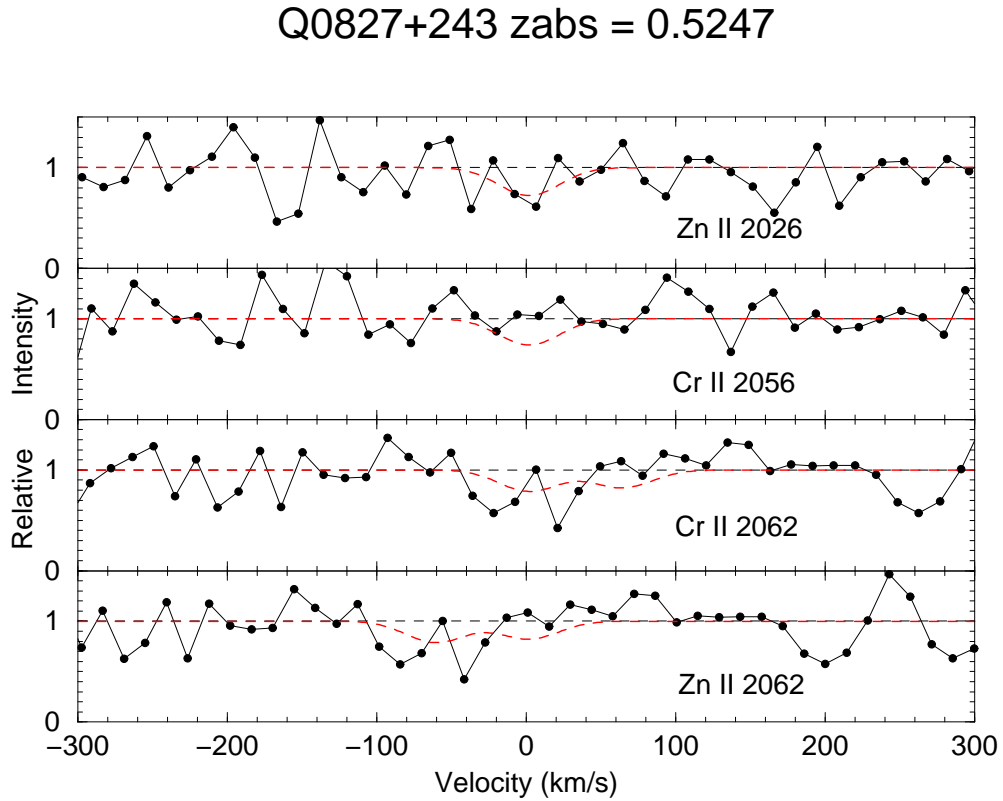


Fig. 10.— Velocity plot of the Zn II and Cr II data for the $z = 0.5247$ DLA toward Q0827+243. The zero point of the velocity scale refers to the absorption redshift $z = 0.5247$ inferred from the 21-cm and optical data. The dashed curves show profiles corresponding to the 3σ upper limits adopted for $b = 10 \text{ km s}^{-1}$.

Q0952+179 zabs = 0.2378

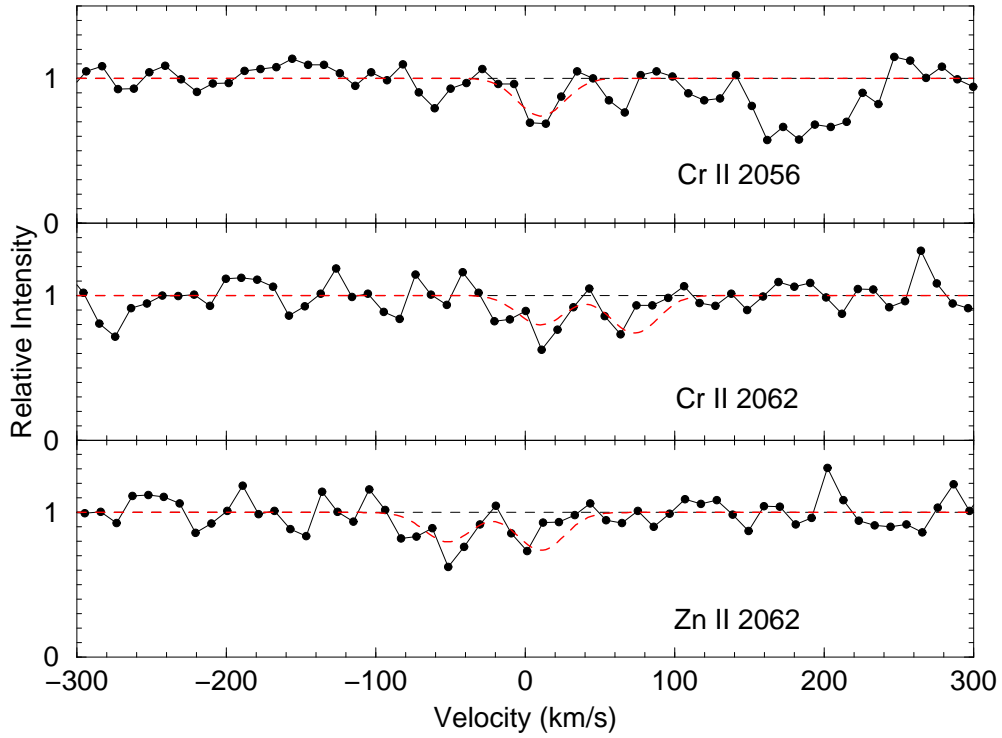


Fig. 11.— Velocity plot of the Zn II and Cr II data for the $z = 0.2378$ DLA toward Q0952+179. The zero point of the velocity scale refers to the absorption redshift $z = 0.2378$ inferred from the 21-cm and optical data. The dashed curves show the profiles for the best-fit N , b , and v parameters obtained by fitting multiple lines simultaneously. In the case of Zn II, the profiles correspond to the 3σ upper limit adopted.

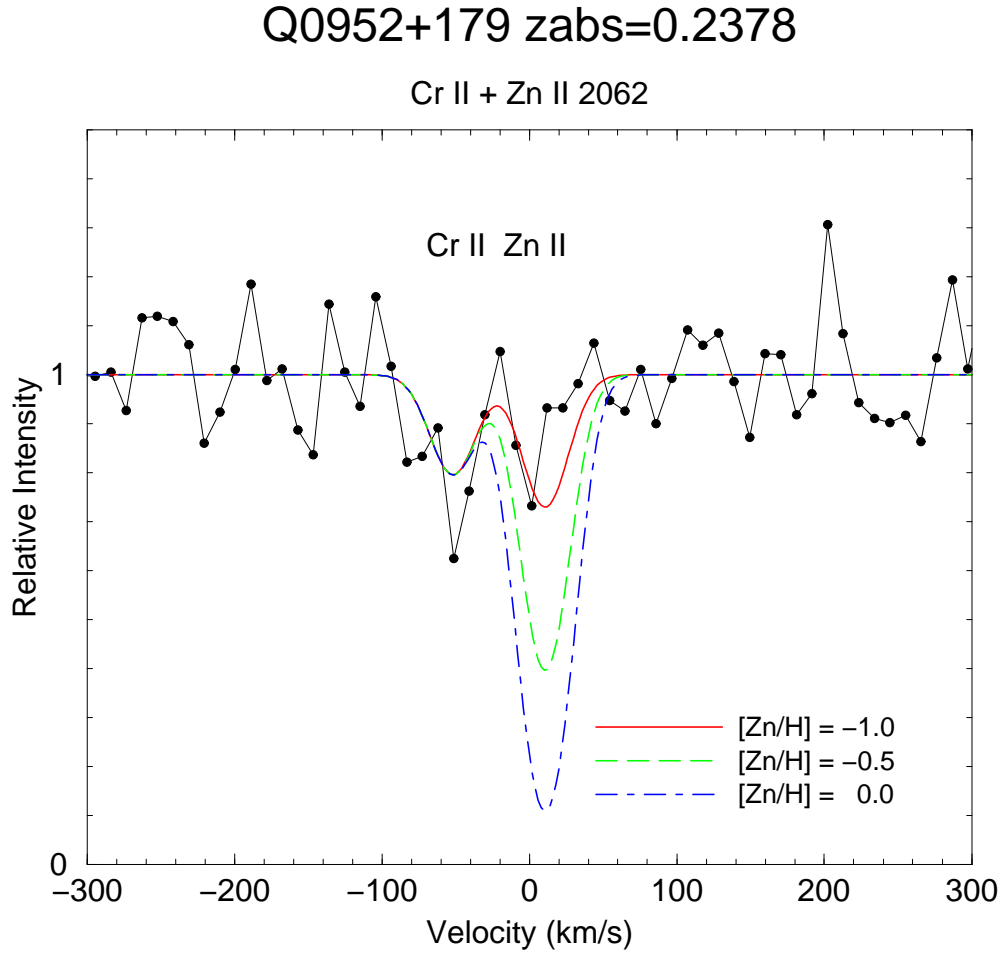


Fig. 12.— Comparison of Zn II $\lambda 2062$ data for the $z = 0.2378$ DLA toward Q0952+179 with simulated Voigt profiles for $[\text{Zn}/\text{H}] = -1.0$, -0.5 , and 0.0 , shown by solid (red), short-dashed (green), and short-dash-long-dashed curves (blue), respectively. All three curves assume the best-fit values of b , v , and Cr II column density obtained by fitting multiple lines simultaneously.

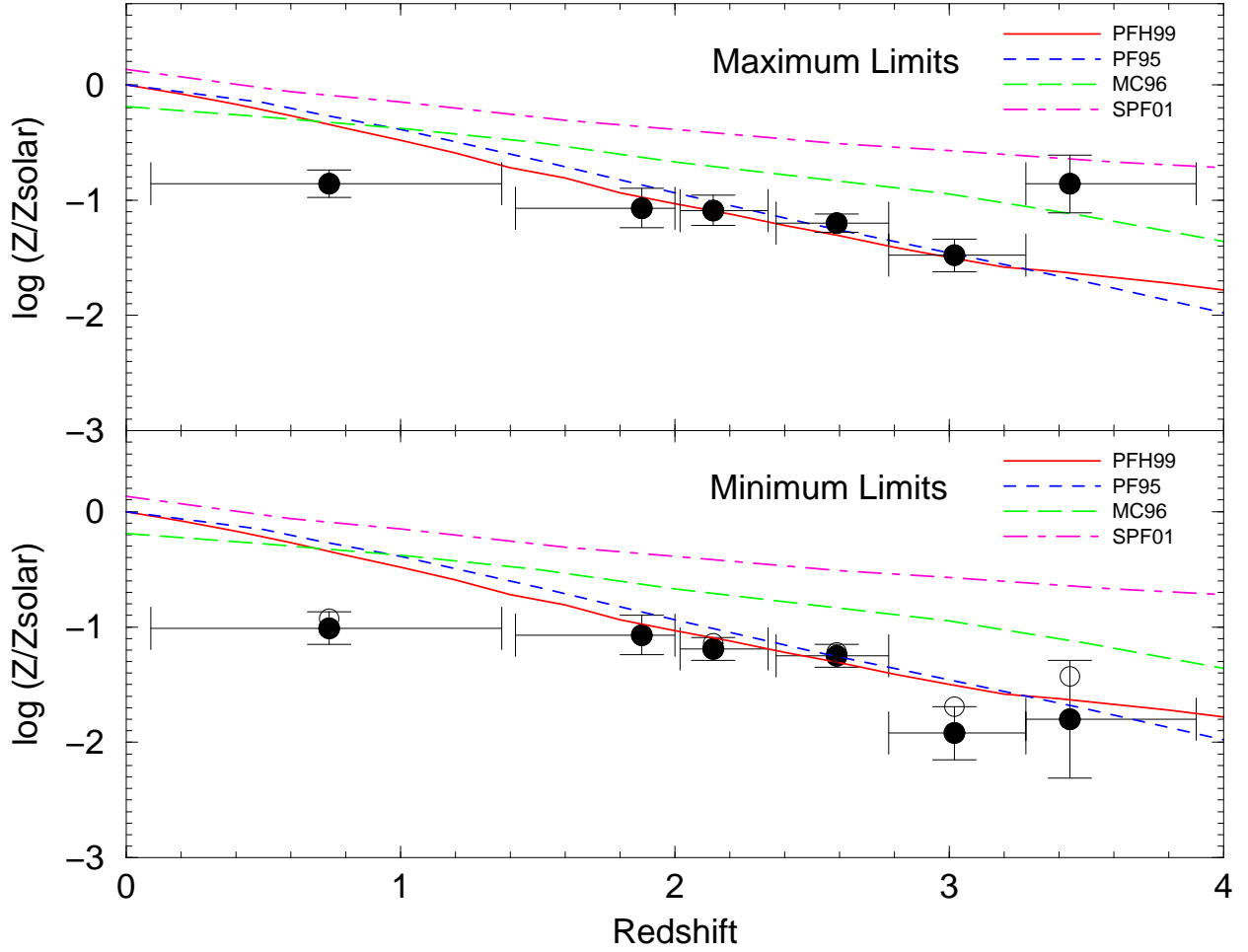


Fig. 13.— The global metallicity-redshift relation deduced from damped Ly- α absorbers. The circles show the logarithm of the $N(\text{HI})$ -weighted mean Zn metallicity relative to the solar value vs. redshift for the sample of 87 DLAs based on our *HST* observations and the literature. The filled circles in the top (a) and bottom (b) panels show, respectively, the $N(\text{HI})$ -weighted mean metallicity for the maximum-limits and minimum-limits cases using Zn only. The unfilled circles in the bottom panel show the $N(\text{HI})$ -weighted mean metallicity for the modified minimum-limits sample, using other elements to constrain the metallicities in cases of Zn limits. Vertical error bars on the filled circles in both panels denote 1σ uncertainties in the logarithm of the $N(\text{HI})$ -weighted mean metallicity. Data points are plotted at the median redshift in each bin. Horizontal bars for each bin extend from the lowest DLA redshift to the highest DLA redshift within that bin. The short-dashed (blue), long-dashed (green), solid (red), and short-dash-long-dashed (magenta) curves show, respectively, the “true” mean metallicity (not corrected for dust obscuration) expected in the cosmic chemical evolution models of Pei & Fall (1995), Malaney & Chaboyer (1996), Pei et al. (1999), and Somerville et al. (2001).

TABLE 1
Target DLAs

QSO	z_{em}	z_{abs}	$\log N_{\text{HI}}$	Ref. [†]
Q0738+313	0.635	0.0912	$21.18^{+0.05}_{-0.06}$	1, 2
Q0738+313	0.635	0.2212	$20.90^{+0.07}_{-0.08}$	1, 3
Q0827+243	0.939	0.5247	$20.30^{+0.04}_{-0.05}$	4, 5
Q0952+179	1.472	0.2378	$21.32^{+0.05}_{-0.06}$	4, 5

[†] References: 1. Rao & Turnshek (1998); 2. Chengalur & Kanekar (1999); 3. Lane et al. (1998); 4. Rao & Turnshek (2000); 5. Kanekar & Chengalur (2001).

TABLE 2
Details of *HST* STIS Observations

QSO	Detector	Grating	R	λ_{cent}	t_{exp} (s)
Q0738+313	NUV-MAMA	G230M	12,100	2176	13,388
Q0738+313	NUV-MAMA	G230M	12,500	2257	11,224
Q0738+313	NUV-MAMA	G230M	13,900	2499	13,613
Q0827+243	CCD	G230MB	10,400	3115	12,232
Q0952+179	NUV-MAMA	G230M	14,300	2579	24,346

TABLE 3
Line Lists

QSO	No.	λ_{obs} (Å)	W_{obs} (Å)	σ_W^p (Å)	ID	z_{abs}
Q0738+313	1 [†]	2155.47	0.140	0.039		
	2 [†]	2187.08	0.157	0.043		
	3	2211.03	0.092	0.027	Zn II 2026	0.0912
	4 [†]	2216.58	0.157	0.039		
	5	2243.99	0.096	0.029	Cr II 2056	0.0912
	6	2260.75	0.180	0.033	Fe II 2260	0.0000
	7	2467.07	0.109	0.028	Fe II 2260	0.0912
	8	2504.76	0.403	0.036	C IV 1548	0.6179
	9	2508.86	0.234	0.030	C IV 1551	0.6178
	10	2518.49	0.061	0.020	Cr II 2062	0.2212
	11	2519.13	0.066	0.017	Zn II 2062	0.2213
Q0952+179	1	2545.32	0.070	0.020	Cr II 2056	0.2378
	2	2546.78	0.234	0.032	Ly- α	1.0950
	3	2552.69	0.100	0.024	Cr II 2062	0.2378
	4	2553.18	0.052	0.021	Zn II 2062	0.2378
	5	2560.01	0.060	0.019	Ly- α	1.1058
	6	2564.45	0.616	0.037	Ly- α	1.1095
	7	2566.22	0.770	0.033	Ly- α	1.1109
	8	2571.61	0.081	0.025	Ly- α	1.1154
	9	2576.78	0.282	0.036	Mn II 2577	0.0003
	10	2586.60	0.843	0.042	Fe II 2586	0.0003
	11	2590.69	0.447	0.044	Ly- α	1.1311
	12	2594.27	0.262	0.039	Mn II 2594	0.0002
	13	2600.21	1.054	0.043	FeII 2600	0.0003
	14	2606.26	0.218	0.040	Mn II 2606	0.0002
	15	2612.30	0.198	0.029	Ly- α	1.1489
	16	2615.42	1.224	0.057	Ly- α	1.1514

† No clear identification, but possibly C IV λ 1548 lines at $z_{abs} = 0.392, 0.413,$ and 0.432 with the corresponding C IV λ 1551 lines lost in noise.

TABLE 4
Further Details on DLA Metal-line Features

QSO	λ_{obs} (\AA)	W_{obs} (\AA)	σ_W^p (\AA)	σ_W^c (\AA)	σ_W^t (\AA)	ID	z_{abs}
Q0738+313	2211.03	0.092	0.027	0.019	0.033	Zn II 2026	0.0912
	2243.99	0.096	0.029	0.020	0.036	Cr II 2056	0.0912
	2467.07	0.109	0.028	0.018	0.033	Fe II 2260	0.0912
Q0738+313	2518.49	0.061	0.020	0.009	0.022	Cr II 2062	0.2212
	2519.13	0.066	0.017	0.008	0.019	Zn II 2062	0.2213
Q0952+179	2545.32	0.070	0.020	0.019	0.028	Cr II 2056	0.2378
	2552.69	0.100	0.021	0.012	0.024	Cr II 2062	0.2378
	2553.18	0.052	0.021	0.013	0.025	Zn II 2062	0.2378

TABLE 5
Column Densities and Abundances for the $z = 0.0912$ DLA toward Q0738+313

Fitting Procedure	b (km s ⁻¹)	$\log N_{\text{CrII}}$ (cm ⁻²)	$\log N_{\text{ZnII}}$ (cm ⁻²)	$\log N_{\text{FeII}}$ (cm ⁻²)	[Cr/H]	[Zn/H]	[Fe/H]
N, b, v varied [†] ; multiple lines	11.2 ± 6.7	$13.28^{+0.14}_{-0.22}$	< 12.66	$15.02^{+0.12}_{-0.17}$	$-1.55^{+0.15}_{-0.23}$	< -1.14	$-1.63^{+0.13}_{-0.18}$
b fixed; single lines	5.0	$13.56^{+0.24}_{-0.56}$	$13.06^{+0.22}_{-0.49}$	$15.22^{+0.21}_{-0.41}$	$-1.27^{+0.25}_{-0.56}$	$-0.75^{+0.23}_{-0.49}$	$-1.43^{+0.22}_{-0.41}$
	10.0	$13.49^{+0.16}_{-0.24}$	$12.84^{+0.13}_{-0.19}$	$15.06^{+0.13}_{-0.20}$	$-1.34^{+0.17}_{-0.25}$	$-0.97^{+0.17}_{-0.20}$	$-1.59^{+0.17}_{-0.21}$
	15.0	$13.48^{+0.14}_{-0.21}$	$12.81^{+0.12}_{-0.17}$	$15.06^{+0.12}_{-0.17}$	$-1.35^{+0.15}_{-0.22}$	$-1.00^{+0.13}_{-0.18}$	$-1.59^{+0.13}_{-0.18}$
	20.0	$13.50^{+0.13}_{-0.19}$	$12.81^{+0.12}_{-0.17}$	$15.06^{+0.12}_{-0.16}$	$-1.33^{+0.17}_{-0.20}$	$-1.00^{+0.13}_{-0.18}$	$-1.59^{+0.13}_{-0.17}$

[†] For the fits with N, b, v varied, the error bars on column densities and abundances include uncertainties from Poisson statistics and uncertainties in b value, central velocity, and continuum placement. The limits are 3σ upper limits.

TABLE 6
Column Densities and Abundances for the $z = 0.2212$ DLA toward Q0738+313

Fitting Procedure	b (km s ⁻¹)	$\log N_{\text{CrII}}$ (cm ⁻²)	$\log N_{\text{ZnII}}$ (cm ⁻²)	[Cr/H]	[Zn/H]
N, b, v varied [†] ; multiple lines ^{††}	12.2 ± 7.5	$13.11^{+0.15}_{-0.24}$	$12.83^{+0.12}_{-0.16}$	$-1.44^{+0.17}_{-0.25}$	$-0.70^{+0.14}_{-0.17}$
b fixed; single lines	5.0	$13.22^{+0.16}_{-0.25}$	$12.75^{+0.15}_{-0.24}$	$-1.33^{+0.18}_{-0.26}$	$-0.78^{+0.17}_{-0.25}$
	10.0	$13.20^{+0.14}_{-0.20}$	$12.73^{+0.13}_{-0.18}$	$-1.35^{+0.16}_{-0.21}$	$-0.80^{+0.15}_{-0.19}$
	15.0	$13.21^{+0.13}_{-0.19}$	$12.76^{+0.12}_{-0.17}$	$-1.34^{+0.15}_{-0.20}$	$-0.77^{+0.14}_{-0.18}$
	20.0	$13.23^{+0.13}_{-0.19}$	$12.80^{+0.12}_{-0.16}$	$-1.32^{+0.15}_{-0.20}$	$-0.73^{+0.14}_{-0.17}$

†: For the fits with N, b, v varied, the error bars on column densities and abundances include uncertainties from Poisson statistics and uncertainties in b value, central velocity, and continuum placement. ††: The noisy data at the positions of the $\lambda 2026$ and $\lambda 2056$ lines are not included in these fits, but they give consistent results of $\log N_{\text{ZnII}} < 12.81$ and $\log N_{\text{CrII}} < 13.37$, respectively for the best-fit b value of 12.2 km s^{-1} . Nevertheless, to be conservative, we finally adopt an upper limit $[\text{Zn}/\text{H}] \leq -0.70$ for this system.

TABLE 7
Column Densities and Abundances for the $z = 0.5247$ DLA toward Q0827+243

Fitting Procedure	b (km s ⁻¹)	$\log N_{\text{CrII}}$ (cm ⁻²)	$\log N_{\text{ZnII}}$ (cm ⁻²)	[Cr/H]	[Zn/H]
b fixed; single lines [†]	5.0	< 13.79	< 13.23	< -0.16	< 0.30
	10.0	< 13.51	< 12.89	< -0.44	< -0.04
	15.0	< 13.45	< 12.83	< -0.50	< -0.10
	20.0	< 13.42	< 12.80	< -0.53	< -0.13

[†] The limits are 3σ upper limits.

TABLE 8
Column Densities and Abundances for the $z = 0.2378$ DLA toward Q0952+179

Fitting Procedure	b (km s ⁻¹)	$\log N_{\text{CrII}}$ (cm ⁻²)	$\log N_{\text{ZnII}}$ (cm ⁻²)	[Cr/H]	[Zn/H]
N, b, v varied [†] ; multiple lines	15.0 ± 7.7	$13.32^{+0.12}_{-0.17}$	< 12.93	$-1.65^{+0.14}_{-0.18}$	< -1.02
b fixed; single lines	5.0	13.30 ± 0.20	12.62 ± 0.20	-1.67 ± 0.21	-1.33 ± 0.25
	10.0	13.24 ± 0.20	12.62 ± 0.20	-1.73 ± 0.21	-1.33 ± 0.25
	15.0	13.25 ± 0.20	12.66 ± 0.20	-1.72 ± 0.21	-1.29 ± 0.25
	20.0	13.26 ± 0.20	12.71 ± 0.20	-1.71 ± 0.21	-1.24 ± 0.25

[†]: For the fits with N, b, v varied, the error bars on column densities and abundances include uncertainties from Poisson statistics and uncertainties in b value, central velocity, and continuum placement. The limits are 3σ upper limits.

TABLE 9
Summary of Abundances

QSO	z_{abs}	[Zn/H]*	[Cr/H]*	[Fe/H]	Ref.†
Q0738+313	0.0912	< -1.14	$-1.55^{+0.15}_{-0.23}$	$-1.63^{+0.13}_{-0.18}$	1
Q0738+313	0.2212	≤ -0.70	$-1.44^{+0.17}_{-0.25}$...	1
Q0827+243	0.5247	< -0.04	< -0.44	-1.02 ± 0.05	1, 2
Q0952+179	0.2378	< -1.02	$-1.65^{+0.14}_{-0.18}$...	1

*: Values obtained from fits with N , b , v varied simultaneously for multiple lines.

† References: 1. This Work; 2. Khare et al. (2004).

TABLE 10
Summary of Zn Measurements in DLAs

QSO	Ref. [†]	z_{abs}	[Zn/H]	$N_{\text{HI}}/10^{20}(\text{cm}^{-2})$	$N_{\text{ZnII}}/10^{12}(\text{cm}^{-2})$
0738+313	1	0.0912	≤ -1.14	15.00 ± 2.00	≤ 4.59
0738+313	1	0.2212	≤ -0.70	7.90 ± 1.40	≤ 6.69
0952+179	1	0.2378	≤ -1.02	21.00 ± 2.50	≤ 8.55
1229-021	2	0.3950	-0.45	5.62 ± 0.91	8.51 ± 2.38
0827+243	1	0.5247	≤ -0.04	2.00 ± 0.20	≤ 7.75
1122-1649	3	0.6819	≤ -1.29	2.82 ± 0.99	≤ 0.61
3c286	4	0.6922	-1.20	19.50 ± 2.25	5.27 ± 1.47
1107+0048	5,6	0.7404	-0.60	10.00 ± 0.75	10.72 ± 1.24
0454+039	7	0.8596	-0.99	4.90 ± 0.68	2.14 ± 0.32
1727+5302	5	0.9449	-0.52	14.50 ± 4.35	18.62 ± 1.91
0302-223	7	1.0093	-0.54	2.29 ± 0.59	2.82 ± 0.14
1727+5302	5	1.0312	-1.39	26.00 ± 7.80	4.47 ± 0.46
0515-44	3	1.1500	-0.95	2.82 ± 1.00	1.36 ± 0.13
0948+43	8	1.2330	-0.95	31.62 ± 7.35	15.14 ± 0.00
0935+417	9	1.3726	-0.78	2.50 ± 0.50	1.76 ± 0.41
1354+258	10	1.4200	-1.58	34.67 ± 4.81	3.89 ± 0.97
0933+733	5	1.4790	-1.58	42.00 ± 8.00	4.68 ± 1.47
1104-180A	11	1.6614	-0.99	7.08 ± 0.16	3.08 ± 0.07
1151+068	12	1.7736	-1.53	20.00 ± 5.00	2.50 ± 0.50
1331+170	13	1.7764	-1.26	15.00 ± 1.42	3.48 ± 0.23
2314-409	14	1.8573	-1.01	7.94 ± 1.85	3.31 ± 0.77
2230+025	15	1.8642	-0.68	7.08 ± 1.38	6.31 ± 0.41
1210+1731	13	1.8920	-0.86	3.98 ± 0.92	2.34 ± 0.16
2206-199	13	1.9205	-0.37	4.50 ± 0.74	8.20 ± 0.17
1157+014	16	1.9440	-1.34	63.10 ± 14.66	12.30 ± 2.28
0551-366	17	1.9620	-0.11	3.16 ± 0.59	10.47 ± 1.21
0013-004	18	1.9733	-0.72	6.70 ± 0.70	5.47 ± 0.50
1850+44	19	1.9900	-0.68	25.12 ± 5.84	22.39 ± 5.20
1215+333	13,15	1.9990	-1.25	8.91 ± 1.38	2.14 ± 0.24
0010-002	8	2.0250	-1.16	6.31 ± 1.47	1.86 ± 0.28
0458-020	13,15	2.0395	-1.15	44.67 ± 9.32	13.61 ± 0.63
2231-00	15	2.0660	-0.73	3.63 ± 0.84	2.90 ± 0.15
0049-283	20	2.0713	≤ -1.04	3.10 ± 0.40	≤ 1.22
2206-199	13	2.0762	≤ -1.86	2.70 ± 0.37	≤ 0.16
2359-02	15	2.0950	-0.73	5.00 ± 1.16	3.94 ± 0.26
0149+33	15	2.1400	-1.64	3.16 ± 0.73	0.31 ± 0.08
0528-250	21	2.1410	-1.45	8.91 ± 1.03	1.35 ± 0.45
2359-02	15	2.1540	≤ -1.03	2.00 ± 0.46	≤ 0.80

TABLE 10. Summary of Zn Measurements in DLAs (cont'd)

QSO	Ref. [†]	z_{abs}	[Zn/H]	$N_{\text{HI}}/10^{20}(\text{cm}^{-2})$	$N_{\text{ZnII}}/10^{12}(\text{cm}^{-2})$
1451+123	22	2.2550	-1.08	2.00 ± 0.70	0.71 ± 0.18
2348-147	15,20	2.2789	≤ -1.28	3.63 ± 0.63	≤ 0.82
0216+080	23	2.2931	≤ -0.27	2.82 ± 1.06	≤ 6.46
PHL957	15	2.3091	-1.54	25.10 ± 2.90	3.12 ± 0.17
2243-6031	24	2.3300	-1.08	4.68 ± 0.22	1.66 ± 0.12
1232+0815	25	2.3376	-0.84	8.00 ± 1.00	4.90 ± 1.60
0841+129	15	2.3745	-1.47	8.91 ± 1.80	1.30 ± 0.15
0112+029	20	2.4227	-1.13	9.00 ± 2.00	2.86 ± 0.82
2343+12	26	2.4310	-0.74	2.24 ± 0.26	1.73 ± 0.05
0836+113	13	2.4651	≤ -1.09	3.80 ± 0.88	≤ 1.32
1223+178	13	2.4658	-1.58	31.62 ± 7.35	3.55 ± 0.21
CTQ247A	27	2.5505	-1.32	13.49 ± 3.13	2.75 ± 0.32
1209+093	28	2.5840	-1.05	25.12 ± 5.84	9.59 ± 1.17
CTQ247B	27	2.5950	-1.04	12.30 ± 2.86	4.79 ± 0.22
2348-011	13	2.6145	≤ -2.06	19.95 ± 4.63	≤ 0.74
0913+072	12	2.6183	≤ -1.09	2.30 ± 0.40	≤ 0.80
1759+75	29	2.6250	-1.05	5.77 ± 0.09	2.20 ± 0.42
0812+32	28	2.6260	-0.95	22.40 ± 5.20	10.80 ± 0.55
Ctq460	28	2.7770	≤ -1.27	10.00 ± 2.32	≤ 2.29
0056+014	12	2.7771	-1.20	13.00 ± 2.00	3.50 ± 2.00
1253-025	28	2.7830	-1.71	70.79 ± 33.77	5.86 ± 1.00
1132+2243	28	2.7830	≤ -1.64	10.00 ± 1.62	≤ 0.97
1337+113	28	2.7950	≤ -1.38	8.91 ± 2.07	≤ 1.59
2138-444	8	2.8520	-1.48	6.31 ± 1.17	0.89 ± 0.21
2342+34	28	2.9080	-1.23	12.59 ± 0.29	3.17 ± 0.80
1021+3001	28	2.9490	≤ -1.14	5.01 ± 1.16	≤ 1.55
0426-2202	28	2.9830	≤ -1.97	31.62 ± 11.14	≤ 1.46
0347-383	30	3.0250	-0.96	3.63 ± 0.42	1.70 ± 0.20
2334-09	28	3.0570	≤ -0.91	2.82 ± 0.65	≤ 1.47
0808+52	28	3.1130	≤ -1.15	4.47 ± 0.72	≤ 1.36
1535+2943	31	3.2020	≤ -0.75	4.47 ± 1.57	≤ 3.40
2344+0342	28	3.2190	≤ -1.71	22.39 ± 3.62	≤ 1.85
2315+0921	31	3.2190	≤ -2.03	22.39 ± 7.89	≤ 0.89
1506+522	28	3.2240	≤ -1.20	4.68 ± 0.76	≤ 1.27
1432+39	28	3.2720	≤ -1.23	17.78 ± 4.13	≤ 4.42
0957+33	28	3.2800	≤ -0.95	2.82 ± 0.52	≤ 1.35
2239-386	12	3.2810	≤ -1.01	5.75 ± 1.01	≤ 2.40
2155+1358	28	3.3160	≤ -1.13	3.55 ± 1.25	≤ 1.13

TABLE 10. Summary of Zn Measurements in DLAs (cont'd)

QSO	Ref. [†]	z_{abs}	[Zn/H]	$N_{\text{HI}}/10^{20}(\text{cm}^{-2})$	$N_{\text{ZnII}}/10^{12}(\text{cm}^{-2})$
1715+3809	31	3.3410	≤ -1.57	11.20 ± 3.47	≤ 1.30
1117-1329	32	3.3504	-1.21	6.92 ± 1.70	1.81 ± 0.12
0000-263	33	3.3901	-2.03	25.70 ± 4.76	1.02 ± 0.12
1802+5616	31	3.3910	≤ -0.53	2.00 ± 0.46	≤ 2.54
0007+2417	31	3.4960	≤ -1.34	12.60 ± 2.92	≤ 2.45
1802+5616	31	3.5540	≤ -0.50	3.16 ± 0.74	≤ 4.29
1723+2243	28	3.6950	-0.62	3.16 ± 1.11	3.22 ± 1.07
1248+31	28	3.6960	≤ -0.65	4.27 ± 0.69	≤ 4.12
1535+2943	31	3.7610	≤ 0.08	2.51 ± 0.89	≤ 12.90
0133+0400	28	3.7740	≤ -0.08	3.55 ± 0.98	≤ 12.56
0747+2739	28	3.9000	≤ -0.73	3.16 ± 0.74	≤ 2.50

[†] References: 1. This Paper; 2. Boisse et al. (1998); 3. de la Varga et al. (2000); 4. Meyer & York (1992); 5. Khare et al. (2004); 6. Rao, Turnshek, & Nestor (2004); 7. Pettini et al. (2000); 8. Prochaska et al. (2003b); 9. Meyer et al. (1995); 10. Pettini et al. (1999); 11. Lopez et al. (1999); 12. Pettini et al. (1997); 13. Prochaska et al. (2001b); 14. Ellison & Lopez (2001); 15. Prochaska & Wolfe (1999); 16. Petitjean, Srianand, & Ledoux et al. (2000); 17. Ledoux, Srianand, & Petitjean (2002); 18. Petitjean, Srianand, & Ledoux et al. (2002); 19. Prochaska & Wolfe (1998); 20. Pettini et al. (1994); 21. Centurion et al. (2003); 22. Dessauges-Zavadsky et al. (2003); 23. Lu et al. (1996); 24. Lopez et al. (2002); 25. Ge, Bechtold, & Kulkarni (2001); 26. Dessauges-Zavadsky et al. (2004); 27. Lopez & Ellison (2003); 28. Prochaska et al. (2003c); 29. Prochaska et al. (2002); 30. Ledoux, Petitjean, & Srianand (2003); 31. Prochaska et al. (2003a); 32. Peroux et al. (2002); 33. Molaro et al. (2001).

TABLE 11
Global Zn Metallicity vs. Redshift (Binned)

z range	Med. z	D,L [†]	$\log(\bar{Z}/Z_{\odot})$ Max. Lim. Zn only	$\log(\bar{Z}/Z_{\odot})$ Min. Lim. Zn only	$\log(\bar{Z}/Z_{\odot})$ Min. Lim. Zn+others	$\log(\bar{Z}/Z_{\odot})$ Mean of Max, Min ^{††}	$\log(\bar{Z}/Z_{\odot})$ Surv. Anal.
0.09-1.37	0.74	10, 5	−0.86 ±0.11	−1.01 ±0.14	−0.93 ±0.10	−0.89 ±0.12	−0.94 ±0.16
1.42-2.00	1.88	14, 0	−1.07 ±0.17	−1.07 ±0.17	−1.07 ±0.17	−1.07 ±0.17	−1.07 ±0.16
2.02-2.34	2.14	10, 5	−1.09 ±0.13	−1.19 ±0.10	−1.14 ±0.10	−1.12 ±0.12	−1.16 ±0.23
2.37-2.78	2.59	10, 4	−1.20 ±0.08	−1.25 ±0.10	−1.22 ±0.08	−1.21 ±0.08	−1.21 ±0.14
2.78-3.27	3.02	4, 11	−1.48 ±0.14	−1.92 ±0.23	−1.69 ±0.14	−1.59 ±0.20	−1.65 ±0.19
3.28-3.90	3.44	3, 11	−0.86 ±0.25	−1.80 ±0.51	−1.43 ±0.22	−1.14 ±0.46	−1.30 ±0.15

† D: Number of Zn Detections, L: Number of Zn Limits. ††: The minimum limit value used while calculating this mean is the one with information from other elements used in cases of Zn limits.

TABLE 12
Exponential Fits to Global Metallicity-Redshift Relation

Redshift range	Binning	Treatment of Limits	$\log(\bar{Z}_0/Z_\odot)$	B
0.09-3.90	Binned	Maximum limits	-0.74 ± 0.15	-0.18 ± 0.06
0.09-3.90	Binned	Minimum limits, Zn only	-0.75 ± 0.18	-0.22 ± 0.08
0.09-3.90	Binned	Minimum limits, Zn + others [†]	-0.71 ± 0.13	-0.23 ± 0.06
0.09-3.90	Binned	Mean of Max., Min. Limits [†]	-0.72 ± 0.16	-0.20 ± 0.07
0.09-3.90	Binned	K-M Survival Analysis	-0.79 ± 0.18	-0.18 ± 0.07
0.09-3.28	Binned	Maximum limits	-0.66 ± 0.15	-0.23 ± 0.07
0.09-3.28	Binned	Minimum limits, Zn only	-0.77 ± 0.18	-0.22 ± 0.08
0.09-3.28	Binned	Minimum limits, Zn + others [†]	-0.69 ± 0.14	-0.24 ± 0.06
0.09-3.90	Unbinned	Maximum limits	-0.86 ± 0.15	-0.11 ± 0.08
0.09-3.90	Unbinned	Minimum limits, Zn only	-0.95 ± 0.08	-0.14 ± 0.05
0.09-3.90	Unbinned	Minimum limits, Zn + others [†]	-0.86 ± 0.08	-0.15 ± 0.05

†: Here, the minimum limit calculation refers to the one with information from other elements used in cases of Zn limits.